

Cryogenic microwave link for quantum local area networks

M. Renger,^{1,2,*} S. Gandorfer,^{1,2,†} W. Yam,^{1,2,‡} F. Fesquet,^{1,2} M. Handschuh,^{1,2} K. E. Honasoge,^{1,2} F. Kronowetter,^{1,2,3} Y. Nojiri,^{1,2} M. Partanen,¹ M. Pfeiffer,^{1,2} H. van der Vliet,⁴ A. J. Matthews,⁴ J. Govenius,⁵ R. N. Jabdaraghi,⁵ M. Prunnila,⁵ A. Marx,¹ F. Deppe,^{1,2,6} R. Gross,^{1,2,6,§} and K. G. Fedorov^{1,2,6,§}

¹Walther-Meißner-Institut, Bayerische Akademie der Wissenschaften, 85748 Garching, Germany

²School of Natural Sciences, Technische Universität München, 85748 Garching, Germany

³Rohde & Schwarz GmbH & Co. KG, 81671 Munich, Germany

⁴Oxford Instruments NanoScience, Tubney Woods, Abingdon, Oxon, OX13 5QX, UK

⁵VTT Technical Research Centre of Finland Ltd. & QTF Centre of Excellence, P.O. Box 1000, 02044 VTT, Finland.

⁶Munich Center for Quantum Science and Technology (MCQST), 80799 Munich, Germany

(Dated: August 25, 2023)

Scalable quantum information processing with superconducting circuits is about to advance from individual processors in single dilution refrigerators to more powerful distributed quantum computing systems located in separate cooling units in order to achieve a practical quantum advantage. Hence, realization of hardware platforms for quantum local area networks (QLANs) compatible with superconducting technology is of high importance. Here, we demonstrate a basic prototype for a microwave QLAN based on a cryogenic link connecting two individual dilution cryostats over a distance of 6.6 m with a base temperature of 52 mK in the center. We provide details about the system design, installation, and performance. We employ superconducting coaxial microwave transmission lines to form a quantum communication channel and characterize its potential by demonstrating robust entanglement distribution in the form of two-mode squeezing between remote parties. By preserving entanglement distribution at link temperatures up to 1 K, we experimentally verify the fluctuation-dissipation theorem. Consequently, we demonstrate that our system can form the backbone for future distributed quantum computing applications.

I. INTRODUCTION

Quantum networks are supposed to provide coherent exchange of quantum states between remote parties [1]. In quantum networks at optical carrier frequencies several paradigmatic applications have been realized, such as multimode entanglement swapping [2], long-distance entanglement distribution [3], as well as satellite-to-ground quantum key distribution [4]. Meanwhile, superconducting quantum processors operating at microwave frequencies are among the most promising hardware platforms for implementing quantum computing applications due to major breakthroughs demonstrating quantum advantage [5] and quantum error correction beyond the break-even point [6, 7]. However, in order to achieve a quantum advantage in relevant practical problems, one needs to increase the number of superconducting qubits to multiple millions [8]. This goal will be extremely hard to achieve within the limited experimental space provided by modern cryostats because of their spatial and cooling limitations, as well as other drawbacks caused by the growing qubit crosstalk on large quantum chips. A possible near-term solution is based on employing a large number of smaller individual superconducting quantum computing units coherently linked together within a quantum local area network (QLAN) [9–14]. Unfortunately, the

large frequency mismatch of about five orders of magnitude between the microwave and optical carrier frequencies [15–17] and the low efficiency of frequency conversion schemes do not allow us to use existing optical techniques for interfacing superconducting qubits. Direct quantum communication at microwave frequencies can provide a solution. Here, recent experiments with propagating quantum microwaves have demonstrated the feasibility of quantum communication in the GHz range [12, 18–21]. Related experimental protocols employ various superconducting waveguides for quantum channels. These waveguides are typically cooled to millikelvin temperatures in order to minimize the influence of thermal noise on the quantum properties of propagating microwave signals. By connecting remote dilution cryostats with a cryogenic link containing such superconducting waveguides, one can realize a quantum link, which can be used for fundamental Bell tests [21] or towards building a prototype microwave QLAN.

In this paper, we demonstrate the realization of a 6.6 meter long cryogenic link connecting two dry dilution refrigerators, acting as quantum communication nodes referred to as “Alice” and “Bob”, located in separate laboratories. A schematic illustration of the system is shown in Fig. 1(a). The center of the link consists of a cold node which we refer to as “Eve” in the following. The construction of Eve also enables the connection of additional link arms for a potential QLAN extension. Consequently, the cryogenic link represents a hardware backbone for a square lattice QLAN unit cell, as shown in Fig. 1(b). We implement a 6 meter long microwave quantum channel in the innermost section of the cryo-

* michael.renger@wmi.badw.de

† M. R., S. G. and W. Y. contributed equally

‡ rudolf.gross@wmi.badw.de

§ kirill.fedorov@wmi.badw.de

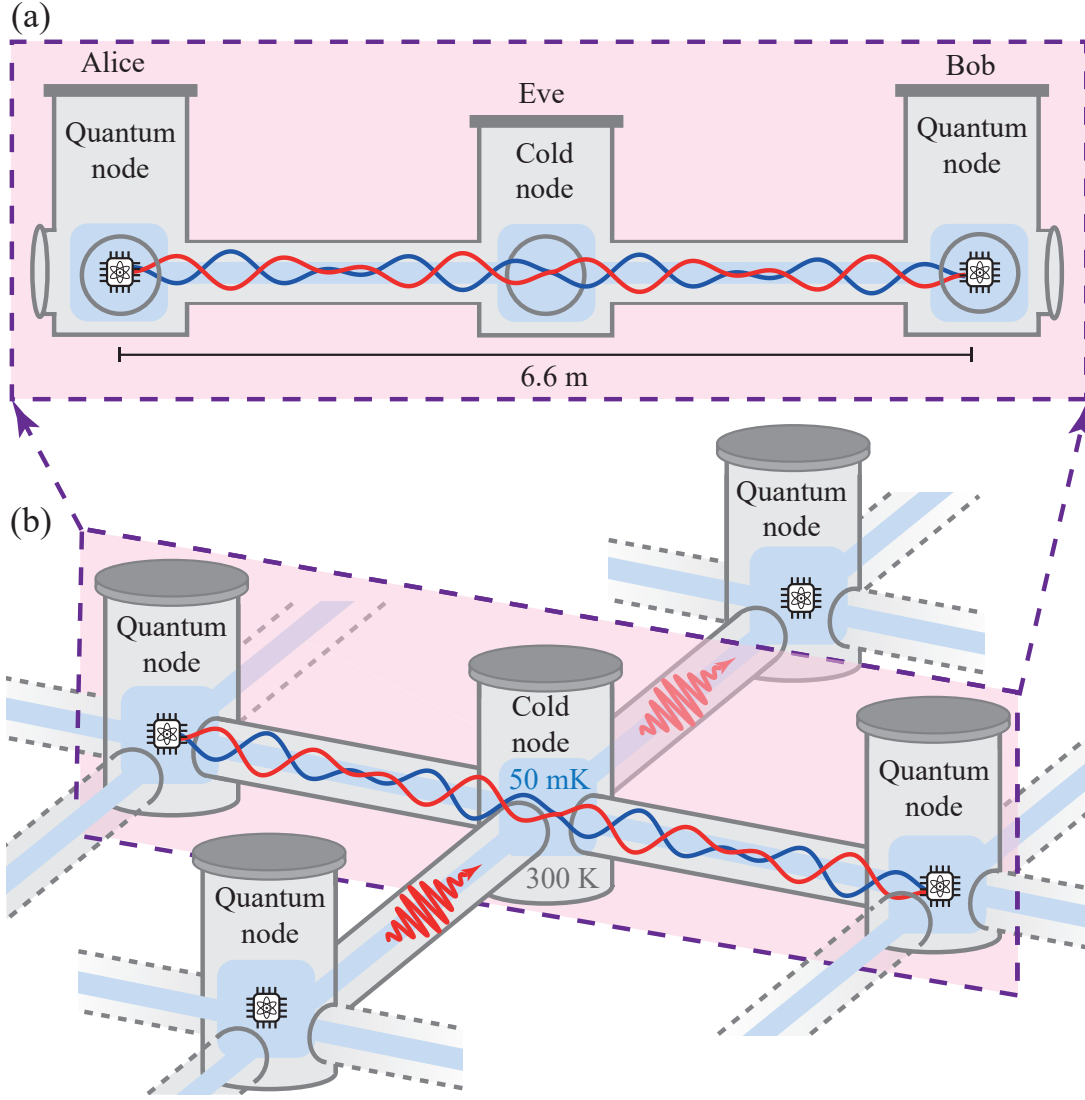


Figure 1. (a) Cryogenic link consisting of two quantum nodes (“Alice”, “Bob”) and the cold node (“Eve”). (b) Schematic illustration of a square lattice QLAN unit cell based on the developed cryogenic link. Four quantum nodes within one plaquette are connected to each other via the cold node.

genic link by using three superconducting coaxial cables. We present the system design and installation as well as its operation and performance. We find that the transmission line is sufficiently long and (intentionally) weakly thermally coupled to enable localized heating of its center without a significant impact on base temperatures of Alice and Bob. Consequently, our cryogenic link can be interpreted as a microwave thermal channel. Its properties can be studied in the framework of quantum communication and, more particularly, entanglement distribution. We experimentally realize the transfer of squeezed microwave states with squeezing levels up to $S = 2.1$ dB below vacuum. We demonstrate the distribution of Gaussian path entanglement over the cryogenic link, between Alice and Bob, and experimentally show robustness of entanglement generation towards the microwave channel temperature. This finding implies that the inner elec-

tromagnetic modes of the superconducting transmission line are decoupled from Eve’s thermal bath, as long as temperature gradients do not affect Alice or Bob directly and we are sufficiently far below the critical temperature, in accordance with the fluctuation-dissipation theorem [22, 23]. As an important technological consequence, preserving quantum coherence in such a system does not necessarily require millikelvin temperatures everywhere along the link, provided a sufficiently high critical temperature and low microwave losses of the employed superconducting cables. The successful microwave entanglement distribution demonstrates that our system can be straightforwardly used for continuous-variable quantum communication between macroscopically remote dilution cryostats and quantum circuits therein.

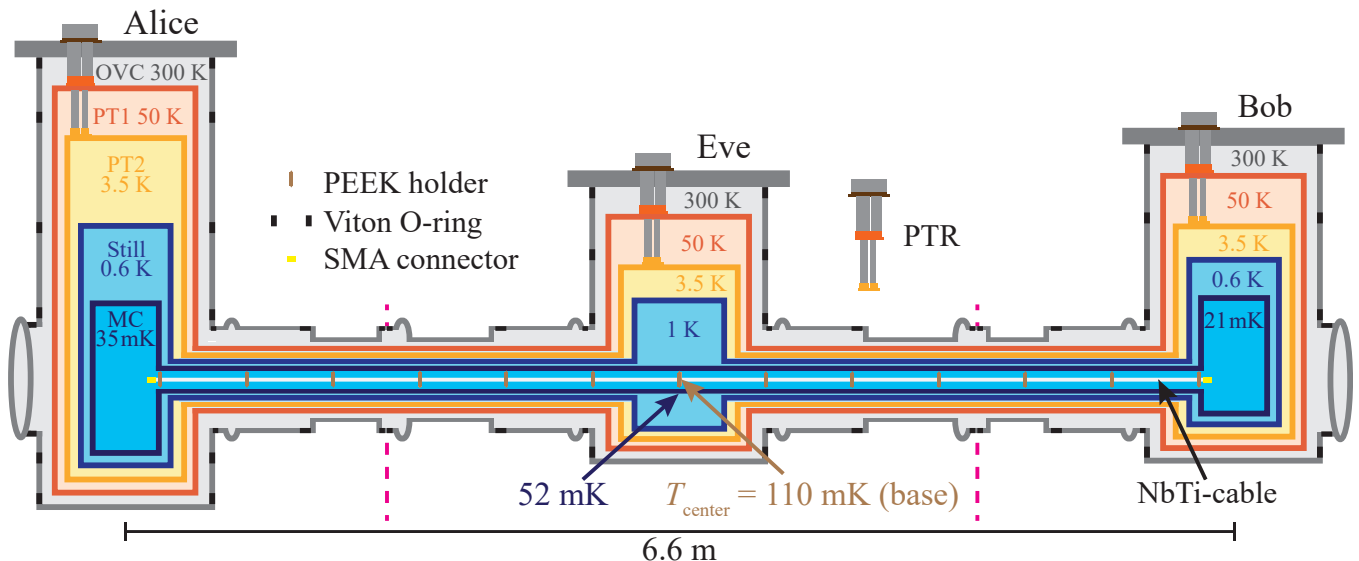


Figure 2. Schematic illustration of the cryogenic link connecting two dry dilution refrigerators, Alice and Bob, spaced apart by 6.6 m. The center of the cryogenic link contains three superconducting coaxial transmission lines forming the microwave quantum channel. Eve, a third cryostat without a dilution unit, supports cooling of the two outermost radiation shields (at temperatures of 50 K and 3.5 K, respectively) of the cryogenic link via an additional pulse tube cooler.

II. CRYOGENIC MICROWAVE LINK

In this section, we describe installation, operation, and performance of the cryogenic link. The link has been designed and assembled in collaboration with Oxford Instruments Nanoscience (OINT) and connects a home-built (at the Walther-Meiner-Institut) dry dilution refrigerator (Alice) [24] with a commercial OINT Triton500 cryostat (Bob). Alice is operated with a Cryomech PT420 pulse tube refrigerator (PTR). Bob and Eve are equipped with respective PT415 PTRs. The shield structure of the cryogenic link coincides with that of the individual Alice and Bob cryostats as schematically illustrated in Fig. 2. Each link arm consists of two segments and is connected to a commercial OINT cryostat (Eve) which does not have a $^3\text{He}/^4\text{He}$ dilution cooling circuit and acts as the cold node. The radiation shields in the cryogenic link are attached to the respective cryostat shields via semicylindrical adapter shells. In this regard, the link is designed with a sufficient mechanical freedom along its symmetry axis to enable flexible attachment while simultaneously guaranteeing a good thermal contact. In order to ensure vacuum tightness and be able to attain a background pressure around 1×10^{-6} mbar, we employ Viton O-ring vacuum seals between room temperature counterparts of the cryolink. Radiation shields corresponding to different temperature stages are thermally separated from each other via fiberglass spacers and designed with sufficient mechanical flexibility to mount the link arms. The entire system is designed with multiple degrees of freedom to enable *in-situ* adjustment of a relative orientation between Alice, Bob, Eve, and the cryogenic link arms. Photographs as well as details re-

garding system design and installation are provided in Appendix A.

The center tube has an inner diameter of 5.2 cm and is attached to the mixing chamber (MC) stages of Alice and Bob. The tube contains three 6 meter long superconducting transmission lines, each formed by combining three 2 meter long coaxial niobium-titanium cables [25]. The transmission lines are free-floating along the link axis inside the MC tube and are thermally decoupled from the tube. In the center of the transmission line, at the position of Eve, we install a RuO_2 thermometer and a heater. Since thermal coupling to Alice and Bob is small due to the low thermal conductivity of the superconducting coaxial cable, the center temperature T_{center} of the transmission line can be stabilized at an elevated temperature of up to 1 K by using an external proportional-integral-derivative (PID) control without significantly affecting the MC temperatures of Alice and Bob. In this way, the cryogenic link enables realization of a microwave thermal channel. More technical information about the transmission lines can be found in Appendix B. An important property of the transmission line is its attenuation α per unit length. We find $\alpha = 2.1 \text{ dB km}^{-1}$ at the carrier frequency of 6 GHz, demonstrating negligibly small dielectric losses, as determined in separate experiments (see Appendix C for more details).

A complete cooldown of the cryogenic link takes approximately 80 h. In order to reach temperatures around $\simeq 10$ K, we employ separate precooling helium circuits in Alice and Bob, as well as a helium-based heat switch in Eve [26]. Precooling of the in-flowing $^3\text{He}/^4\text{He}$ mixture is realized via a Joule-Thompson stage in Bob [27] and a dry 1 K pot in Alice [24]. After the complete cooling pro-

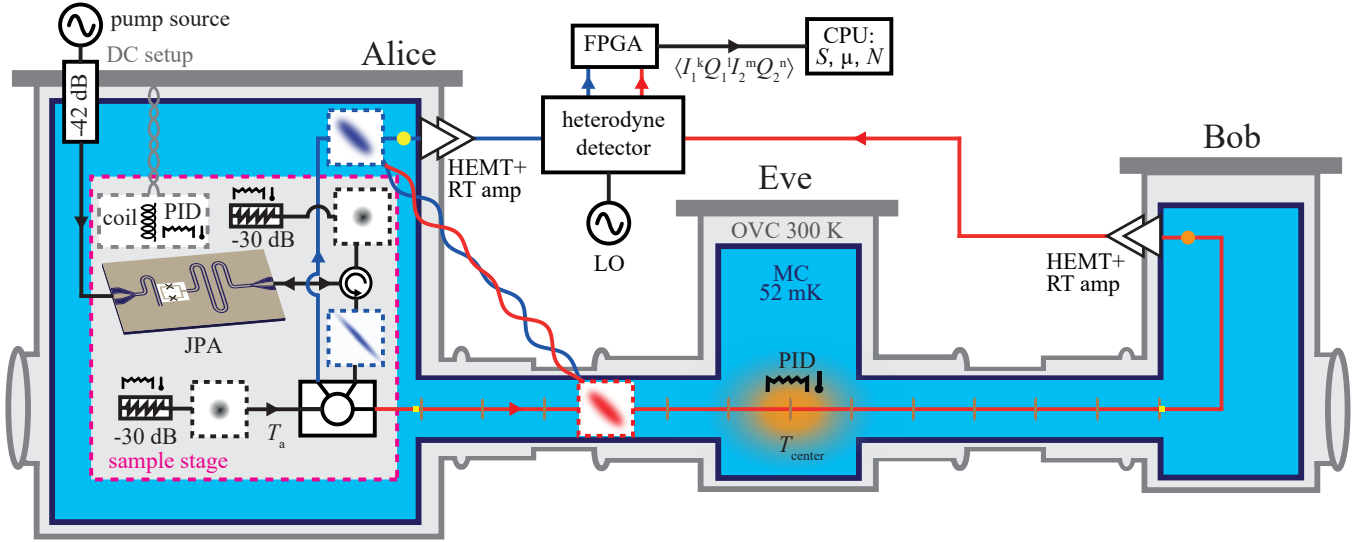


Figure 3. Experimental scheme for quantum state transfer and entanglement distribution over the cryogenic link. Alice contains a flux-driven JPA which implements squeezing of a weak thermal input state. The resulting squeezed state is symmetrically split by a 50 : 50 hybrid ring beam splitter. The output modes of the beam splitter are entangled and broadened by incident fluctuations, corresponding to temperature T_a , at the second beam splitter input port. One of these output modes is kept locally in the Alice lab while the second mode is transmitted over the cryogenic link to the Bob lab. Both modes are reconstructed with a joint tomography. The yellow (orange) dot labels the reconstruction point on Alice’s (Bob’s) side. We repeat the experiment for multiple PID-stabilized temperatures of the transmission line center up to $T_{\text{center}} = 1$ K.

cedure, we reach a lowest temperature of 52 mK in the center of the MC tube. Alice and Bob reach a lowest temperature of 35 mK and 21 mK at the MC stage, respectively. In the center of the transmission line, we detect a steady-state temperature of 110 mK. This elevated temperature, as compared to the MC tube, results from an interplay between black-body radiation in the system and weak thermal anchoring of the transmission line. This black-body radiation is suspected to leak into the system via a gap in the center of the MC tube. This gap emerges from the subdivision of the MC tube into two mechanically independent segments which are plugged into each other and allow for compensation of thermal contraction (see Appendix A). Typical steady-state temperatures of the other cryostat stages are indicated in Fig. 2. Further details about the cooldown procedure as well as about the system performance are provided in Appendix D.

III. SQUEEZED STATE TRANSFER AND ENTANGLEMENT DISTRIBUTION

In the next step, we demonstrate that we can employ our cryogenic link for squeezed state transfer and continuous-variable entanglement distribution between Alice and Bob. The experimental setup is schematically depicted in Fig. 3 and consists of a flux-driven Josephson parametric amplifier (JPA) mounted at the mixing chamber stage of Alice. This JPA has been fabricated at VTT Technical Research Centre of Finland Ltd and consists of a superconducting $\lambda/4$ resonator termi-

nated by a dc-SQUID to the ground. The dc-SQUID provides the Josephson nonlinearity and enables flux-tuning of the JPA resonance frequency, ω_0 [28]. In the following, we choose the state reconstruction frequency $\omega_0/2\pi = 5.65$ GHz. By applying a strong coherent pump field with frequency satisfying the three-wave mixing condition, $\omega_p = 2\omega_0$, the JPA realizes a squeezing operation for the input state [29–31]. We measure the JPA in reflection, where input and output modes are separated by a cryogenic circulator. More details about the samples used in this paper, are provided in Appendix E. The input line of the JPA contains a 30 dB attenuator with PID-controllable temperature T_a which we employ for photon number calibration by Planck spectroscopy [32]. The output signal of the JPA is sent to a hybrid ring acting as a balanced microwave beam splitter. One of the resulting output modes is kept locally in the Alice lab while the second mode propagates to the Bob lab via the superconducting transmission line in the cryogenic link. Both modes are amplified with a cryogenic high electron mobility transistor (HEMT) amplifier and subsequently by multiple amplifiers at room temperature. The amplified signal is finally down-converted to 11 MHz in a heterodyne detection scheme located in the Alice lab [19, 33, 34]. The resulting signals are digitally demodulated and filtered in a field-programmable gate array (FPGA), which enables detection of the statistical quadrature moments $\langle I_1^k Q_1^l I_2^m Q_2^n \rangle$ [18]. These moments are used to reconstruct a resulting two-mode Wigner function in the Gaussian approximation. We use the resulting tomograms in order to determine quantum state

parameters, such as squeezing levels or entanglement monotones [35, 36]. In addition, we use the cryogenic link to implement a tunable thermal channel and repeat the squeezed state transfer experiment for various center temperatures up to $T_{\text{center}} = 1$ K. This approach enables us to experimentally study the impact of thermal noise on the properties of transferred quantum states. Our experimental results from the quantum state transfer as a function of T_{center} are plotted in Fig. 4. Figure 4(a) shows the squeezing level S for the transmitted mode, defined as a relative suppression of the squeezed variance $(\Delta Q_s)^2$ below vacuum, $S = -10 \log_{10} [(\Delta Q_s)^2 / 0.25]$. Each curve corresponds to a fixed JPA pump power and S_0 labels the squeezing level at a base temperature, corresponding to $T_{\text{center}} = 110$ mK. Since the second input port of the hybrid ring broadens the respective variance of the output modes by at least half the amount of vacuum fluctuations [32], the output squeezing level is fundamentally bound by $S \leq -10 \log_{10} 2 \simeq 3$ dB. As can be seen in Fig. 4(a), we measure maximal $S_0 = 2.11 \pm 0.06$ dB, which demonstrates that we can employ our cryogenic link for the successful quantum state transfer. We observe that for $T_{\text{center}} \lesssim 0.4$ K, S is approximately temperature independent, whereas we observe a monotonic decrease of S for higher center temperatures.

We can relate this decrease to the fact that for sufficiently large T_{center} we start warming up Alice's sample stage, leading to an increase of the attenuator temperature, T_a . Consequently, the JPA input state and the state coupled to the second port of the hybrid ring can no longer be approximated to be vacuum. Instead, these states correspond to thermal quantum mixtures obeying Planck statistics, implying that each mode carries $n_{\text{th}}(\omega, T) = 1 / \{\exp[\hbar\omega / (k_B T)] - 1\}$ photons. The Planck formula connects the flat quantum-limited saturation regime $n_{\text{th}}(\omega, T) \rightarrow 0$ in the limit $T \rightarrow 0$ with the linear classical Johnson-Nyquist regime $n_{\text{th}}(\omega, T) = k_B T / (\hbar\omega)$ for $k_B T \gg \hbar\omega$ [32]. As a loss-independent quantifier for the transition between these two curvature-free regimes, we employ the temperature $T_\kappa = 0.22\hbar\omega / k_B$ at which the Planck curve shows maximal curvature, satisfying $\partial_T^3 n_{\text{th}}(\omega, T) = 0$. For our chosen JPA frequency, we find $T_\kappa \simeq 60$ mK. Within this paper, we quantify the quantum saturation regime by $T \lesssim T_\kappa$, as the threshold T_κ is more stringent than alternative quantifiers, such as the crossover temperature $T_{\text{cr}} = \hbar\omega / (2k_B)$ [32]. Consequently, for attenuator temperatures $T_a \gtrsim T_\kappa$, the noise spectral density at the sample stage can be no longer regarded as quantum-limited but contains a noticeable thermal contribution which we need to take into account in our state reconstruction scheme.

In case we neglect the gain-dependent JPA noise [34], the squeezed variance at the beam splitter output is given by

$$(\Delta Q_s)^2 = \frac{1 + 2n_{\text{th}}(\omega_0, T_a)}{8} (e^{-2r} + 1), \quad (1)$$

where r denotes the squeeze factor of the state at the

beam splitter input. Detection of squeezing $S > 0$ requires $n_{\text{th}} \leq 1/2$, implying $T_a \leq \hbar\omega_0 / (k_B \ln 3) \simeq 0.243$ K. Figure 4(d) shows the measured dependence of T_a on T_{center} and we observe that $T_a \lesssim T_\kappa$ for $T_{\text{center}} \lesssim 0.4$ K. Since we simultaneously satisfy $T_{\text{center}} \gg T_\kappa$, we can conclude that, apart from direct heating of the sample stage, the thermal bath, corresponding to T_{center} , does not strongly interact with the transferred squeezed state. This effect becomes more clear when looking at the state purity $\mu = 1 / \sqrt{16 \det \mathbf{V}}$, where \mathbf{V} denotes a reconstructed covariance matrix associated with the transmitted quantum state. Purity measures a deviation of the state uncertainty from the Heisenberg limit and consequently provides an estimate of quantum statistical mixing with environment [37]. As can be seen in Fig. 4(b), μ is approximately independent of T_{center} , as long as $T_a \lesssim T_\kappa$, implying that quantum coherence is preserved despite the thermal nature of the transmission channel.

To determine entanglement between Alice's local mode and the transmitted mode, we estimate the negativity N for the final two-mode covariance matrix [36, 38]. Negativity is an entanglement monotone based on the Peres-Horodecki PPT criterion [39]. Positive values of negativity, $N > 0$, imply path entanglement between corresponding modes (between Alice and Bob in our case). While neglecting losses and a gain-dependent JPA noise, we have $N = \max[(10^{S/10} - 1)/2, 0]$. Consequently, any positive squeezing level gives rise to entangled output modes. Figure 4(d) shows the experimentally reconstructed negativity. We find $N > 0$ for the entire parameter space. It is a notable observation that even at $T_{\text{center}} = 1$ K, corresponding to an average of 3.3 thermal photons per mode, we are not affected by the sudden death of entanglement [40, 41]. The latter is expected to occur independently of S in case the injected noise exceeds the threshold of one added thermal noise photon, $n_{\text{th}}(\omega_0, T_{\text{center}}) = 1$, corresponding to $T_{\text{center}} = \hbar\omega_0 / (k_B \ln 2) \simeq 0.385$ K, in case environmental noise would be coupled into our system. This observation experimentally illustrates the fluctuation-dissipation theorem [22], which states that the variance of the voltage fluctuations, $\langle V^2 \rangle$, in the transmission line within the single-side measurement bandwidth B is given by

$$\langle V^2 \rangle = 2\hbar \int_{\omega_0 - B}^{\omega_0 + B} \coth\left(\frac{\hbar\omega}{2k_B T_{\text{center}}}\right) \varepsilon(\omega) d\omega, \quad (2)$$

where $\varepsilon(\omega)$ corresponds to the dissipation spectrum, determined by the Fourier-transformed voltage susceptibility of the system [23]. For the superconducting cable, the dissipation spectrum is determined by its ohmic resistance. Consequently, we have $\varepsilon(\omega) \rightarrow 0$ for frequencies well below the gap frequency ($\omega_\Delta / 2\pi \simeq 370$ GHz for NbTi), implying that Eq. (2) becomes independent of T_{center} and the thermal environment does not couple to the propagating squeezed state. This temperature-independence holds as long as the cable temperature remains well below the critical temperature of the super-

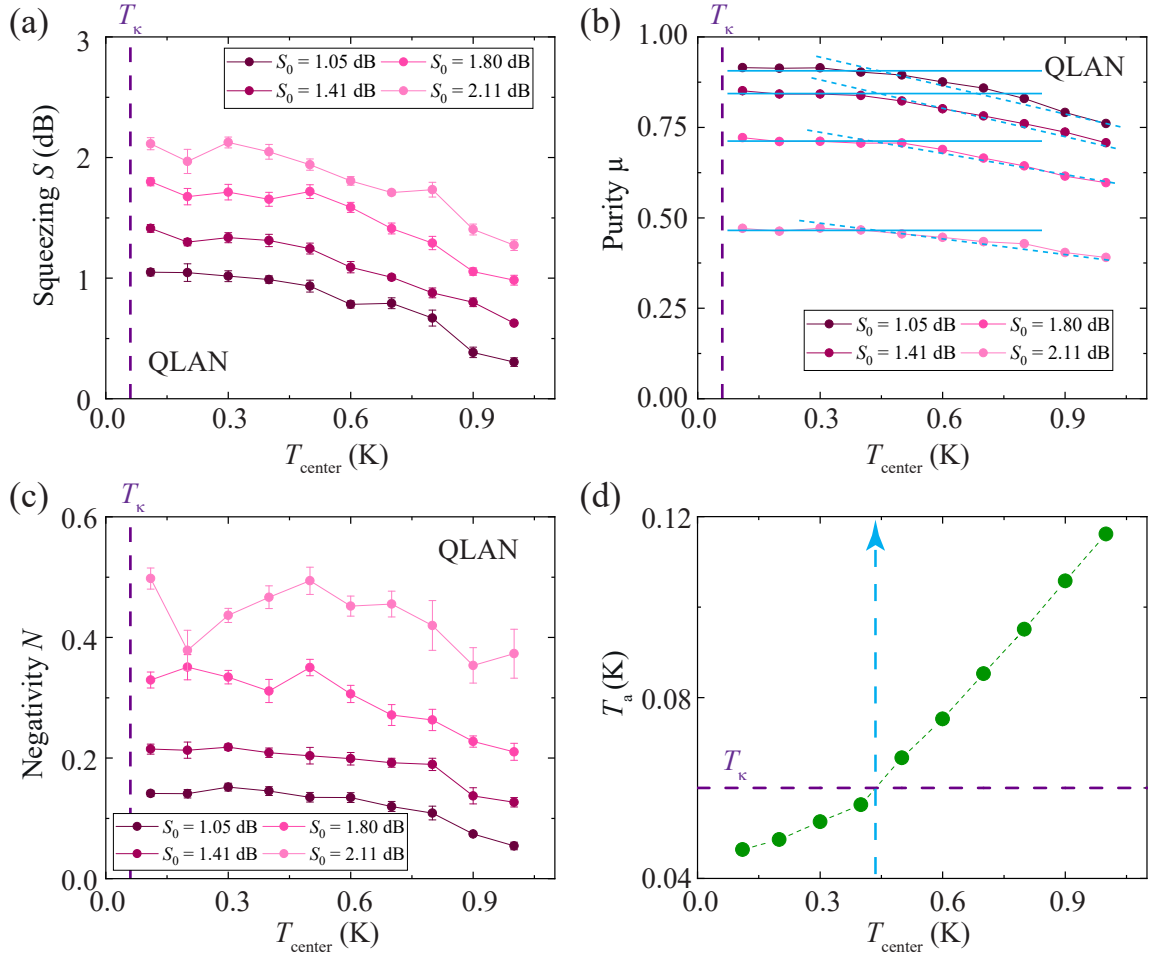


Figure 4. (a) Squeezing level S as a function of the stabilized center temperature, T_{center} , of the transmission line. The quantity S_0 corresponds to the squeezing level at the base temperature, $T_{\text{center}} = 110$ mK. The dashed vertical line marks the temperature $T_\kappa = 0.22\hbar\omega/k_B$ (see text). (b) Purity μ of the transmitted squeezed states. Solid blue lines indicate the flat region corresponding to $T_a \lesssim T_\kappa$. Dashed blue lines indicate decreasing purity in the case $T_a \gtrsim T_\kappa$. (c) Negativity N between Alice's local mode and Bob's mode as a function of T_{center} . We measure $N > 0$ for the entire parameter space, demonstrating successful entanglement distribution between Alice and Bob. (d) Temperature T_a of the heatable attenuator as a function of T_{center} . Finite temperature T_a leads to degradation of S , μ , and N in case T_a exceeds the threshold temperature T_κ . The blue dashed arrow indicates the value of T_{center} corresponding to $T_a = T_\kappa$. Solid and dashed lines connecting data points are a guide to the eye.

conductor, $T_{\text{center}} \ll T_c$. In this case the characteristic thermal energy scale is much smaller than the corresponding gap energy $\Delta(T_{\text{center}})$ of the superconductor, implying that we can neglect the surface resistance of the transmission line, $R_s \propto \exp[-\Delta(T_{\text{center}})/(k_B T_{\text{center}})]$ [42, 43]. Thus, the phononic environmental and photonic mode temperatures of the superconducting cable can be regarded as effectively decoupled from each other and the thermal fluctuation spectrum in the signal line is effectively limited by the input mode temperature T_a . Consequently, although fragile quantum states are transmitted through the thermal bath, interaction between both systems can be neglected.

IV. CONCLUSION AND OUTLOOK

In summary, we have realized a hardware platform for a microwave quantum local area network by connecting two dilution refrigerators, located in separate laboratories, over a distance of 6.6 m via a cryogenic link which reaches a center temperature of 52 mK. The innermost section of our cryogenic link contains three coaxial superconducting transmission lines with respective lengths of 6 meters, each of them forming a microwave quantum channel. We have reached a typical temperature of 110 mK at the center of the transmission lines, which is limited by the interplay of the deliberate weak thermal coupling and residual heat loads. We provide technical details about the system design and assembly as

well as about its operation and performance. We have demonstrated that our system is suitable for establishing a thermal quantum channel with tunable temperature between two distinct laboratories. We have employed our system for a successful transfer of squeezed states with squeezing levels of up to 2.11 ± 0.06 dB. In addition, we have demonstrated the distribution of continuous-variable microwave entanglement between the remote dilution fridges. This entanglement distribution has remained robust when increasing the temperature of the center channel up to 1 K. The corresponding thermal noise significantly exceeds the expected limit for sudden death of entanglement. As a result, our measurements experimentally prove the fluctuation-dissipation theorem by verifying that environmental thermal noise does not affect the fragile squeezed state in the transmission line and corresponding quantum correlations as long as the cable remains in the superconducting state. As an important technical consequence, microwave quantum state transfer and entanglement distribution do not necessarily require millikelvin links but can also be realized at significantly higher temperatures, e.g., corresponding to temperatures of liquid helium, or even liquid nitrogen, as long as the corresponding transmission channel remains in the superconducting state characterized by low absorption losses at microwave frequencies.

As an outlook, the demonstrated cryolink can serve as a versatile platform for many fundamental and applied experiments. One of the most straightforward steps is the implementation of microwave quantum teleportation between distant laboratories and the extension of the QLAN to many quantum nodes by using our scalable architecture for fundamental studies of multipartite entanglement. Furthermore, these experiments can be used for entanglement of remote superconducting qubits with squeezed microwaves, paving the road towards distributed quantum computing [44, 45] and hybrid quantum information processing [46, 47]. More fundamental experiments involve applications for dark matter axion searches [48, 49], where the cryogenic link would allow to separate areas of large magnetic fields, as required in axion detection schemes, and fragile quantum-limited detectors based on superconducting circuits.

Acknowledgements We acknowledge valuable support of Kurt Uhlig regarding modifications of our home-built dilution refrigerator. We acknowledge the work of Janne Lehtinen consisting of the supervision of process development in the cleanroom and room-temperature characterization of the JPAs. We acknowledge Craig Bone for his instrumental work in the build and test of this project, Andy Czajkowski, Anthony Swan, and Tom Marsh for their support during test, Chris Wilkinson for the design of the cryogenic link, Will Dunsby for the welding of the copper MC radiation shield. We acknowledge support by the German Research Foundation via Germany's Excellence Strategy (EXC-2111-390814868), the EU Flagship project QMiCS (Grant No. 820505), the German Federal Ministry of Education and Research via

the project QUARATE (Grant No. 13N15380). This research is part of the Munich Quantum Valley, which is supported by the Bavarian state government with funds from the Hightech Agenda Bayern Plus.

Competing interests

The authors declare no competing interests.

Data availability

The data that support the findings of this study are available from the corresponding author upon reasonable request.

APPENDIX

A. Design and assembly of the cryogenic link

There are multiple engineering considerations and challenges when designing a 6.6 meter long millikelvin link. The length of the system generates problems for alignment, thermal contraction along the link, and large radiative heat loads onto the shields. Each of these constraints and engineered solutions is discussed in this section. Our initial required specifications for the cryogenic link were a base temperature of the new dilution refrigerator (Bob) less than 50 mK, the maximum temperature of the center of the cold node, Eve less than 100 mK, a diameter of at least 50 mm within the mixing chamber shield and the length between Alice and Bob of more than 6 m.

The cryostats - Alice and Bob Alice is a home-built dry dilution cryostat [24], where precooling of the $^3\text{He}/^4\text{He}$ mixture is realized using a pulse tube refrigerator (PTR) and a dry 1 K pot. Bob is a commercial Oxford Instruments Triton500 dilution refrigerator and is equipped with a Cryomech PT415-RM PTR and a Joule-Thompson (JT) impedance. When operated as a stand-alone refrigerator, Bob has a cool down time to a base temperature of 10 mK within less than 24 hours and a temperature stability of ± 0.1 mK at a temperature of 50 mK. Both cryostats are equipped with a customized tailset; a room temperature outer vacuum chamber (OVC), an aluminum radiation shield for the first (PT1) and second (PT2) PTR stages and radiation shields for the still and mixing chamber (MC) stages, manufactured from electropolished copper. To reduce the radiative heat load onto the PT1 shields, those are covered with 40 layers of Mylar superinsulation. Both Alice and Bob are designed with two horizontal ports so that the superconducting cables could be fed through the tailset of one cryostat all the way to the other. A photograph of such a port in the Bob tailset is shown in Fig. 5(c).

The cold network node - Eve The center of the cryogenic link consists of a cold node, Eve. Eve contains a Cryomech PT415-RM PTR to add additional cooling power to the PT1 and PT2 shields in the center of the cryogenic link. In addition, Eve is equipped with a still

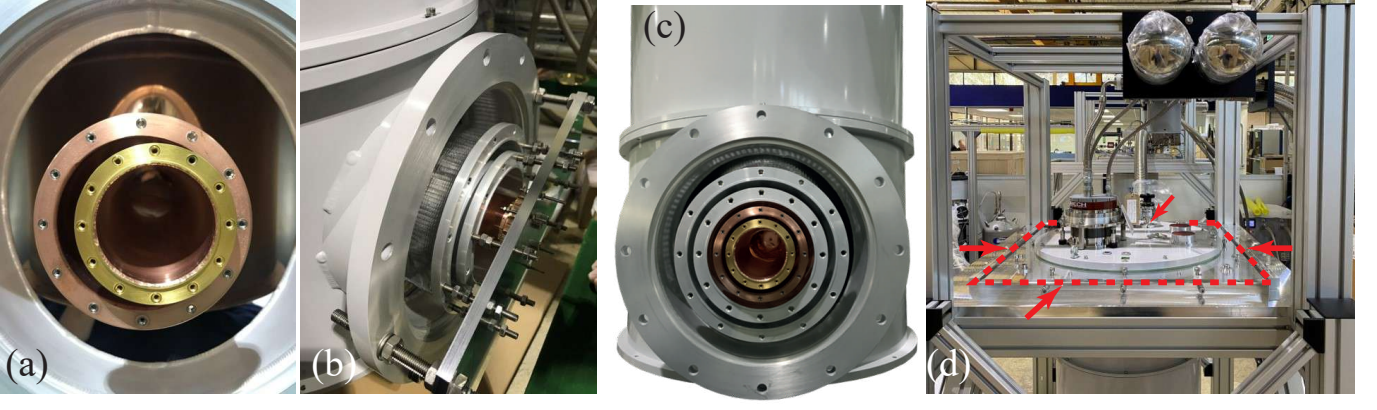


Figure 5. (a) The radiation shields of the cryogenic link before the alignment. (b) Orientation adjustment of the radiation shields. (c) Tailset and connection port for the Bob cryostat. On initial installation, a jig is used to make sure each shield is aligned correctly with respect to the OVC. (d) Alignment top plate on Eve, indicated by the dashed red lines. The red arrows indicate potential movement directions of the plate.

shield but does not have an MC shield. Instead, the MC tube of the cryogenic link is guided directly through Eve’s still stage and mounted from Eve’s still plate with a Kevlar support. Eve is designed with four ports, which allow for future cryogenic links to be added to the system, which could be useful for applications in distributed quantum computing and construction of extended quantum networks. In contrast to Alice and Bob, Eve neither has a dilution unit, nor a JT or 1 K stage, but provides enough internal space for a possible upgrade into a full-fledged dilution cryostat.

The cryogenic link The cryogenic link consists of four segments with a shield structure coinciding with that of the dilution fridges. The four link segments are supported by height-adjustable frames, constructed from profiled aluminium extrusion. Within each segment, the inner radiation shields have support structures that also act as spacers during operation, described in detail below. By having the segments of the cryogenic link rely on the separate frames means that the inner radiation shields never have to be “unnested” and can be connected one by one to the other segments of the link. The innermost tube has a diameter of 5.2 cm and connects the mixing chamber (MC) shield of Alice with Bob’s MC shield. A computer-aided design (CAD) drawing of the system is provided in Fig. 6(a). The drawing shows the OVC shield structure of Alice, Bob and Eve as well as the OVC tube of the cryogenic link, which has a diameter of 20.5 cm. A photograph of the assembled cryogenic link is shown in Fig. 6(b).

System alignment To align the cryogenic link and associated cryostats (across three separate laboratories) such that the entire system is vacuum leak tight, requires multiple solutions. Prior to mounting the link, a laser-assisted alignment of Alice, Bob, and Eve is performed. The individual cryostat shields are then aligned with respect to their vacuum cans, as shown in Fig. 5(c). Figure 5(a) shows the Bob connection port before align-

ment and Fig. 5(b) shows the alignment jig. The support frames for Bob and Eve are designed with an adjustable top plate. These top plates are equipped with adjusting screws and bars which allow for movement along horizontal and vertical axes (and corresponding rotations if adjustments are made in opposition). Figure 5 (d) shows the alignment top plate from the Eve cryostat. The overall spatial orientation of Alice can be controlled by adjusting the respective air pressure of the three pneumatic bearings for Alice’s support frame [24].

Installing the cryogenic link Prior to the alignment procedure, we need to mount the shields on all three individual cryostats. All respective port covers on Alice, Bob, and Eve need to be removed. In order to connect the arms of the link, creating the thermal connection from the cryostats to the cryogenic link, the bottom base plates of all the shields and the OVC must be removed. This is due to the fact that the mixing chamber arm as well as the still arm are connected from the inside of the mixing chamber shield of Alice and Bob. The PT1 and PT2 arms are connected from the outside of the radiation shields meaning that they can be attached once the system is closed. For connection, we mount cylindrical adapter shells with diameters matched to the respective tube size of the cryogenic link arm, as indicated in Fig. 7(a). Then, we connect the cryogenic link arms using two respective half cylinder shells per shield. Each inner radiation shield is split in two halves to enable access to the innermost sections. The remaining gap between respective shells is covered with aluminum tape to reduce radiative heat leaks. For mounting the MC tube, we employ molybdenum washers to create a thermal contraction mismatch with respect to the employed stainless steel screws, which keeps the connection tight at cryogenic temperatures. A photograph of such an attached half cylinder shell for the MC shield is provided in Fig. 7(b). Figure 7(c) shows the complete connection of the MC arm to the Bob cryostat. The PT1 connection

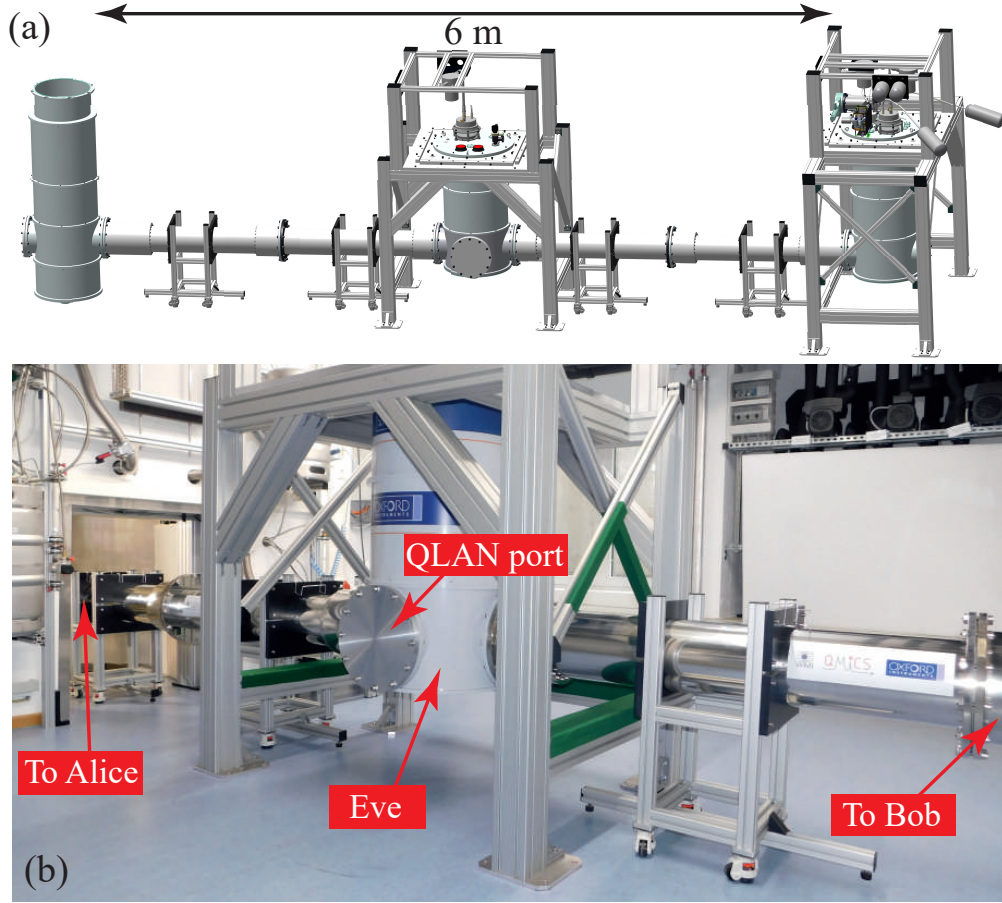


Figure 6. (a) CAD model of the cryogenic link and the respective vacuum shields of Alice, Bob and Eve. (b) Photograph of the central portion of the assembled cryogenic link.

shells are additionally covered with 40 layers of Mylar superinsulation, as can be seen in Fig. 7(d). For ease of connection, the OVC adapter sections use sliding seals, meaning that one can easily access the screws on the inner radiation shields by sliding off the OVC sections. We close the OVC adapters using O-ring seals. For future scalability, the cryostat shields contain additional orifices for potential connection of more link arms. For now, we close these holes with blanks. As an example, such an additional connection port for Eve can be seen in Fig. 6(b) and allows for potential extension of the system. After closing and evacuating the system, a mass spectrometer leak detector demonstrated a ^4He leak rate of $< 5 \times 10^{-8} \text{ mbar l s}^{-1}$.

Link movement on cooldown The length of the cryogenic link between the two dilution refrigerators results in a thermal contraction of the inner shields of the order of 1 cm along the link axis during cooling down. Additionally, the standard cryostat radiation shields contract vertically during cool down (by 1–2 mm). Without suitable mitigation such contractions would damage the cryostat tails. The vertical contraction is addressed by ensuring sufficient clearances for the arms of the link to be off-set at room temperature – the shields become coaxial as the

system cools. These offsets (calculated and designed into the tails) are different for each cryostat as the respective heights of the tails are different [Fig. 6(a)]. Along the length of the link, the PT1, PT2 and still stages, have edge welded bellows included to compensate for the expected contraction of the shields. These edge welded bellows are manufactured from stainless steel and allow for sufficient movement to compensate for thermal contraction (thermalization of the link will be discussed in the following section). Figure 7(e) shows the edge welded bellows stacked concentrically as they would be in the link. Figure 7(f)-(h) depicts the respective bellows for the PT1, PT2, and still stages. The MC temperature tube consists of two independent segments with an overlapping (sliding fit) section at the center of the link. As the shield contracts, the sliding section takes up any length change without exerting forces on the mixing chambers of the dilution refrigerators.

Heat distribution over the cryogenic link At low temperatures, stainless steel is not a good thermal conductor. Along the horizontal direction of the cryogenic link, we need significant heat transfer so that the center of the cryogenic link remains as cold as possible. To ensure that the stainless steel bellows are acting as flexible sec-

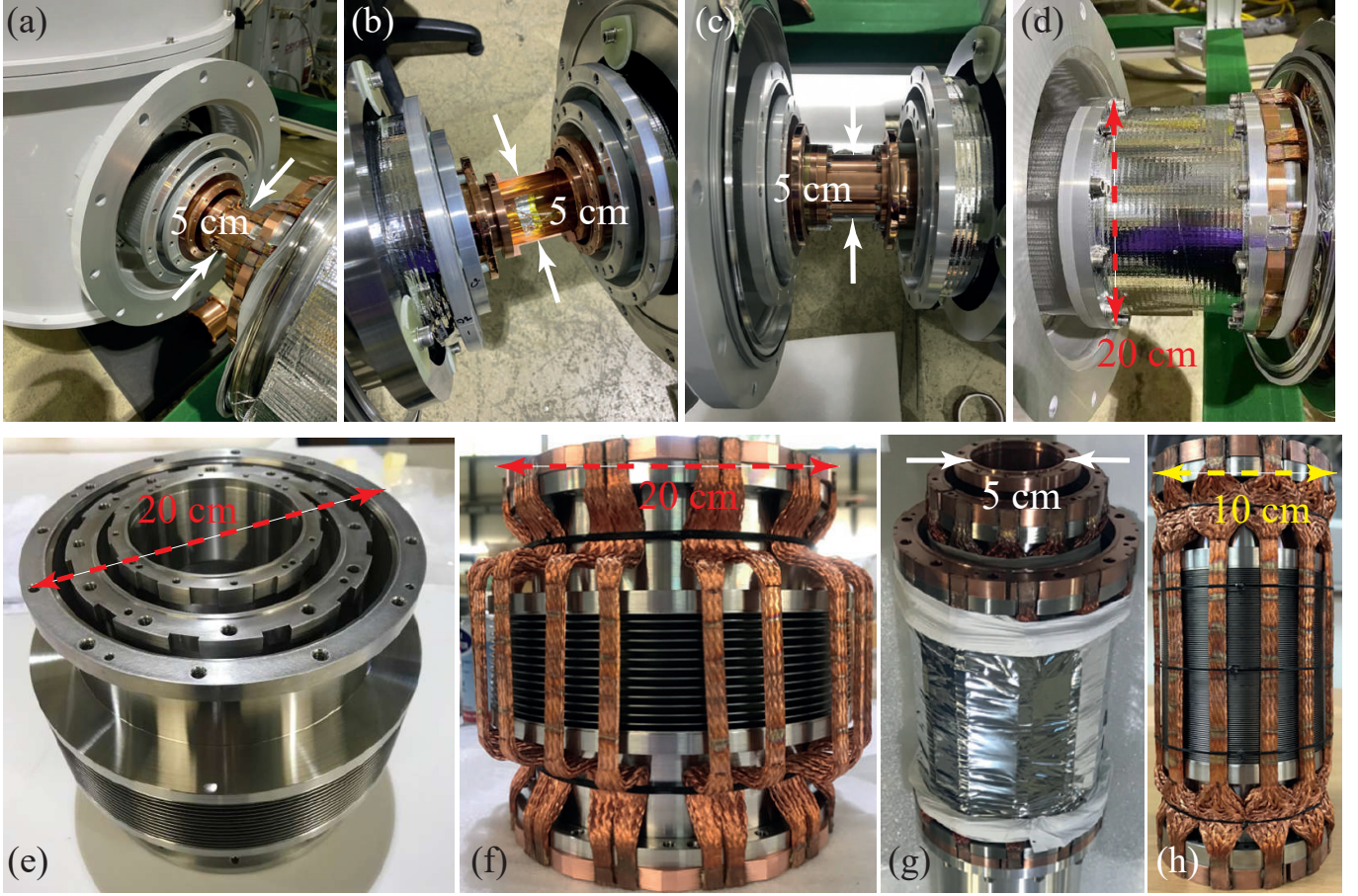


Figure 7. Illustration of various steps of the cryogenic link connection procedure. Panel (a) shows Bob's connection ports together with the to-be-connected link arm. Panel (b) shows a semicylindrical connection shell of the MC section. Panel (c) shows the MC section fully closed. Panel (d) depicts the PT1 shield closed and covered with multilayer insulation. Panel (e) shows edge-welded bellows for the PT1, PT2, and still shields. Panels (f), (g), and (h) illustrate the PT1, PT2, and still connection stages, respectively, showing the copper flanges and copper braid assemblies enabling thermal coupling across the stainless steel bellows.

tions, but not as thermal insulators, copper flanges and copper braids are mounted around the bellows. These copper components can be seen in Fig. 7(f)-(h). The mixing chamber radiation shield does not employ bellows. In order to optimize for minimal temperature in the center of the cryogenic link, the mixing chamber radiation shield is constructed from high-purity, annealed oxygen free high conductance (OFHC) copper. The MC tube is divided into two separate sections which form a sliding connection at the center of Eve. To achieve a uniform heat transfer over the entire tube, both sections are thermally connected by annealed silver wires. To prevent thermal shorts between the different temperature sections of the radiation shields within the cryogenic link, we employ rigid spacers. These spacers are required to consist of insulating, low thermal conductivity material to prevent heat transfer from the hotter radiation shields to colder ones. Determining the heat loads conducted to inner (colder) shields through the spacers requires knowledge of the (temperature dependent) thermal conductiv-

ity of the spacer material, the geometry of the spacer, and the inclusion of contact resistances. Given the complex shape of these spacers, analytic expressions for these values were not expected to be found, instead a finite element analysis using ANSYS software was undertaken. Figure 8(a) shows the CAD model of the cryolink cross section and Fig. 8(b) a photograph of the spacers within each of the radiation shields. Calculations showed that in the 'worst case' configuration of all spacers touching between both the MC and the still shields, there should be no more than a 30 mK temperature increase of the center of the link.

Factory Acceptance Test First, the cryogenic link has been tested in two halves. Two sections of the link (a half link) are tested between Bob and Eve. Standard resistance thermometry is used along the cryogenic link and nuclear orientation thermometry is used for calibration. Figure 9 shows the schematic of the half link tested in the factory at OINT. In its final configuration, each cryogenic half link cools down in 55 hours. The base temperature,

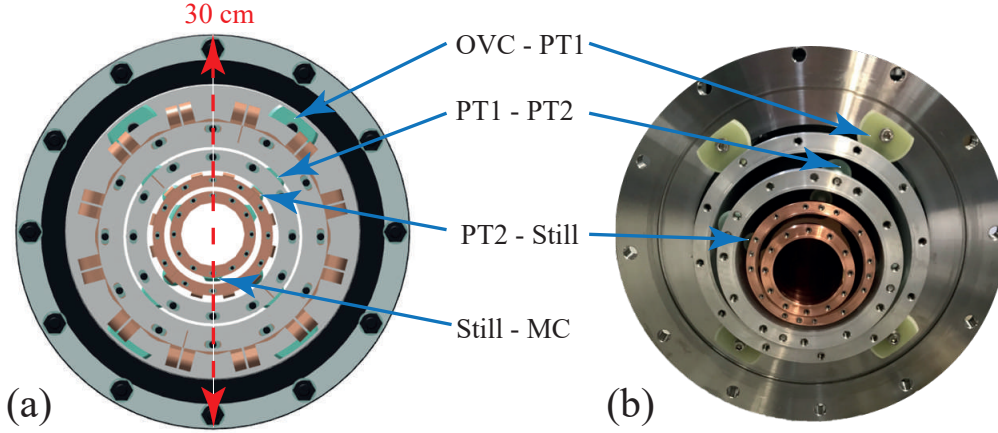


Figure 8. G10 spacers in a cross-section of the cryogenic link. Panel (a) shows the CAD model. Panel (b) shows a port photograph of the actual cryogenic link.

determined with a nuclear orientation thermometer, at the center of Eve, the furthest point from the cooling provided by Bob, was found to be 37 mK.

B. Superconducting transmission line

The MC tube contains three 6 m long continuous superconducting transmission lines forming a microwave quantum channel. Each transmission line is realized by combining three 2 m long superconducting coaxial NbTi cables. The coaxial cables with superconducting joints for connection are fabricated by KEYCOM Corp. [50] and have an attenuation coefficient $\alpha = 2.1 \text{ dB km}^{-1}$ at 6 GHz, as pointed out in Appendix C. The value of α has been determined by embedding the superconducting joint into a microwave resonator and measuring the resulting quality factor, as described in detail in Appendix C. At a temperature of $T \simeq 100 \text{ mK}$, this value is limited by the properties of the joints. As schematically shown in Fig. 2, our superconducting transmission line is supported by 13 holders which are equidistantly spaced inside the mixing chamber tube at intervals of 0.5 m. The central support structure, positioned directly underneath Eve, is shown in Fig. 10(a). The frame of each support holder consists of polyether ether ketone (PEEK). PEEK has been chosen for its low thermal conductivity at cryogenic temperatures, which thermally decouples the cables from the MC tube. Simultaneously, the rigidity of PEEK guarantees stable support and simplifies fabrication, as compared to alternative low thermal conductivity polymers, such as polytetrafluoroethylene (PTFE) [51]. The top and the bottom of the PEEK holder is tip-shaped to minimize mechanical friction. The superconducting cables are clamped to holders, manufactured from gold-plated OFHC copper. These holders are connected to the PEEK support holders via stainless steel joints. We thermalize the transmission line using two silver wires with a respective diameter of 1.5 mm and a

purity of 99.99%. The silver wires are anchored to the MC plate of Alice and Bob. The thermal coupling of the transmission line to the MC stage of Alice and Bob is sufficiently weak to allow for localized heating at the center, which provides a possibility to realize the thermal microwave quantum channel. For temperature stabilization, we install a PID control architecture, consisting of a 100Ω heater and a RuO_2 thermometer at the central support holder, as shown in Fig. 10(a). We employ time domain reflectometry to determine the SMA connection quality, revealing a typical impedance mismatch of 7Ω with respect to the 50Ω standard. These connectors are visible in Fig. 10(b) for the Bob side of the cryogenic link. The microwave connection to the transmission line on the Alice side prior to connecting the link arm is visible in Fig. 10(c). To determine the effect of thermal expansion for the cryogenic link tubes and the transmission line, we employ the empirical relation

$$\frac{L_T - L_{293}}{L_{293}} = (a + bT + cT^2 + dT^3 + eT^4) \times 10^{-5}, \quad (3)$$

where L_T (L_{293}) denotes the length at temperature T (293°C). The polynomial coefficients a, b, c, d, e are tabulated in literature [52, 53]. The corresponding coefficients for NbTi and OFHC copper for the temperature range $4 - 300 \text{ K}$ are listed in Tab. I. In case we employ Eq. (3) to estimate the thermal contraction for a distance of 6 m, we find a value of 1.99 cm for OFHC copper and 1.12 cm for NbTi. To our knowledge, such an empirical relation is not available for silver. Instead, we determine its thermal contraction by using the Grüneisen theory and express the internal energy E and specific heat C using the Debye model [54, 55]. We define $x_D = \Theta_D/T$, where Θ_D is the Debye temperature. The relative length contraction for a given temperature T , compared to $T = 0 \text{ K}$, can then be approximately expressed as [55]

$$\frac{L_T - L_0}{L_0} = \alpha_T \frac{E(x_D)}{C(x_D)} = \alpha_T \frac{T_D}{x_D} \frac{D_3(x_D)}{4D_3(x_D) - 3B(x_D)}, \quad (4)$$

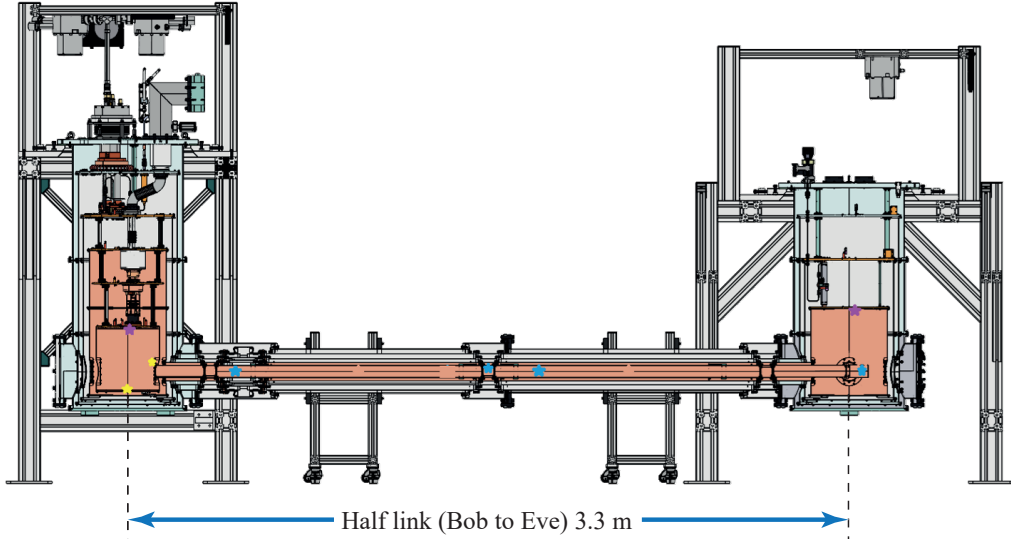


Figure 9. CAD model showing half of the cryogenic link. For the factory acceptance test, sensors are placed at the locations indicated by the stars. Purple stars are the packaged diagnostic ruthenium oxide (RuO_2) sensors on the MC stage of Bob and the 1 K stage of Eve. Blue stars are chip RuO_2 sensors which are attached along the cryogenic link. The yellow stars are packaged RuO_2 sensors, specifically mounted to measure the temperature on the base plate of the MC shield and the adapter flange for the cryogenic link. A nuclear orientation sensor is attached to the end of the MC radiation shield flange in the center of the cryogenic link at Eve.

Table I. Empirical polynomial coefficients for determining the thermal contraction of NbTi and OFHC copper [52, 53].

Sample	a	b	c	d	e
NbTi	-1.862×10^2	-2.568×10^{-1}	8.334×10^{-3}	-2.951×10^{-5}	3.908×10^{-8}
OFHC Cu	-3.317×10^2	-2.037×10^{-2}	6.074×10^{-3}	-7.306×10^{-6}	0

where α_T denotes the linear expansion coefficient at temperature T , $D_3(x)$ is the third Debye function [54] and $B(x) = x/(e^x - 1)$ is the Bernoulli generating function [56]. For copper, the expected thermal contraction according to Eq. (4) is given by 1.95 cm, implying a comparably small deviation of 2.5 % from the result obtained by the empirical relation Eq. (3). For silver, Eq. (4) predicts a contraction of 2.40 cm. To compensate for the thermal contraction of the MC tube, the tube is divided into two parts which are plugged into each other in the center of the cryogenic link. For the radiation shields at higher temperature, thermal contraction is compensated by stainless steel bellows located at the connection of the link arms to the respective cryostats, as described in Appendix A. To account for thermal contraction of the transmission line, the NbTi cables which connect the experimental setup in Alice and Bob to the transmission lines, are bent in an S-shaped way with sufficient margin in length. For the thermal conductivity of PEEK, we employ the empirical relation [57]

$$\lambda_P[\text{W}/(\text{m} \cdot \text{K})] = 18.7 \times T^{1.47} \times 10^{-4}. \quad (5)$$

This relation has been obtained for the temperature range 0.1 – 1 K [57]. In case of silver and NbTi, we additionally neglect the phononic contribution to heat transfer as it follows a cubic temperature dependence well below the Debye temperature and therefore becomes

negligibly small at low T . For our NbTi cables, we take into account that, in the superconducting state, the energy gap $\Delta(T)$ modifies the electronic thermal conductivity λ_n , corresponding to the normal conducting state, since Cooper pairs do not contribute to electronic heat transport [43]. The modified heat conductivity can be expressed as $\lambda_s = y(T)\lambda_n$, where the temperature dependent factor $y(T)$ can be determined within the BCS-theory [58–61]. In the superconducting state, the thermal conductivity is reduced due to the energy gap $\Delta(T)$ in the excitation spectrum, where T corresponds to the effective electronic temperature of the cable. We define the dimensionless parameter $z = \Delta(T)/(k_B T)$ [62]. For a practical calculation of z , we use the interpolation formula [59]

$$z = \delta_{sc} \frac{T_c}{T} \tanh \frac{\pi}{\delta_{sc}} \sqrt{\frac{2}{3} \frac{\Delta C}{C_N} \left(\frac{T_c}{T} - 1 \right)}, \quad (6)$$

with $\delta_{sc} = \pi/e^\gamma$ and $\Delta C/C_N = 12/7\zeta(3)$, where $\gamma = 0.577\dots$ denotes the Euler-Mascheroni constant and $\zeta(3) \simeq 1.202\dots$ is Apéry's constant. According to BCS-theory, the factor y , expressed as a function of z , can be written as [43, 58]

$$y(z) = \frac{3}{2\pi^2} \int_z^\infty \frac{t^2}{\cosh^2\left(\frac{t}{2}\right)} dt, \quad (7)$$

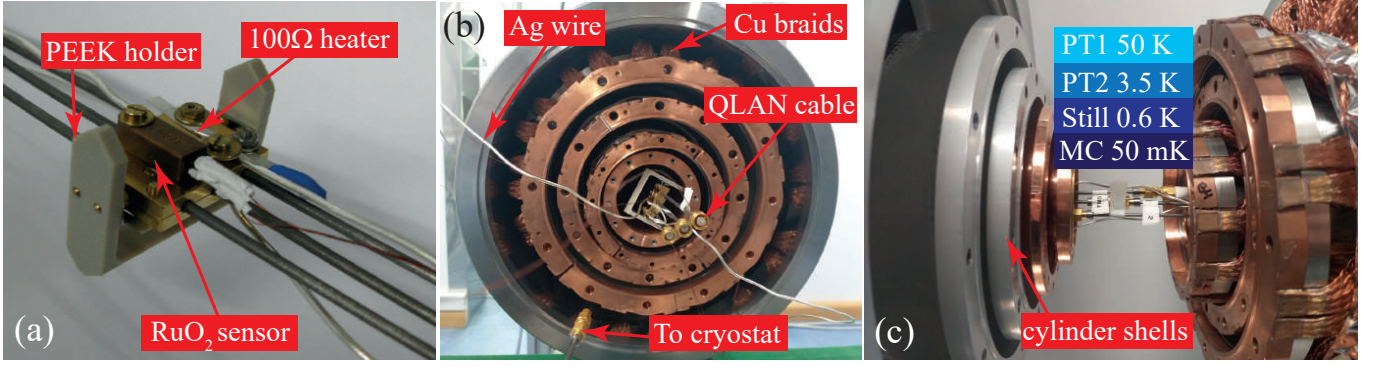


Figure 10. (a) Photograph showing the central support holder for the superconducting transmission line, located inside of Eve. A heater combined with a RuO_2 thermometer is attached to the holder to enable control of the center temperature. (b) Photograph showing the cross section of the shield structure, the silver wires and the crimped SMA connectors of the superconducting transmission lines. (c) Photograph of the established microwave connection with the experimental setup.

which can be analytically expressed as

$$y(z) = \frac{3z}{\pi^2} \left[4 \ln \left(2 \cosh \frac{z}{2} \right) - z - z \tanh \frac{z}{2} \right] - \frac{12}{\pi^2} \text{Li}_2(-e^{-z}), \quad (8)$$

where $\text{Li}_2(x) \equiv -\int_0^x \frac{\ln(1-t)}{t} dt$ denotes the dilogarithm function. For a temperature of 1 K, we estimate a suppression of the thermal conductivity by $y(T) = 4.6 \times 10^{-6}$, where we employ $T_c = 10$ K for the critical temperature of NbTi, leading to a negligible thermal conductivity of $2.3 \times 10^{-6} \text{ W m}^{-1} \text{ K}^{-1}$ [63]. In this temperature regime, the thermal conductivity of the superconducting coaxial cable is eventually determined by the PTFE dielectric [64], which is typically of the order of up to $1 \times 10^{-3} \text{ W K}^{-1} \text{ m}^{-1}$. Consequently, thermalization of the transmission line is determined by the heat conductivity λ_{Ag} of our silver wires. The exact value of λ_{Ag} is not known due to its sensitive dependence on the purity of the material, the annealing, as well as on the quality of the mechanically established thermal contacts. Consequently, we do not know the residual resistivity ratio (RRR) at low temperatures [51]. For a conservative estimation, we assume $\lambda_{\text{Ag}} \simeq 1 \text{ W K}^{-1} \text{ m}^{-1}$. This value is considerably smaller than that measured for high purity silver [51]. In addition, we perform the rough approximation of treating λ_{Ag} as temperature-independent in the limit $T \ll 1$ K.

C. Measurement of transmission line losses

As described previously, each of the three microwave transmission lines inside the cryogenic link consists of three segments of 2 meter long superconducting coaxial NbTi cables, connected to each other by superconducting joints. These joints have been fabricated on demand by KEYCOM Corp. [50]. Microwave losses due to a single joint need to be carefully measured, since they are

expected to be small compared to the losses in other parts of the measurement circuitry, such as connectors. Consequently, it is beneficial to employ a resonator configuration for this task [65]. Figure 11(a)-(d) shows the structure of our resonator setup and the corresponding circuit diagram, and Table II summarizes the main parameters of the resonator. The $\lambda/2$ resonator is capacitively coupled at both ends by coupling capacitors C_κ to the ports 1 and 2 of the external microwave circuit. We can control C_κ by adjusting the gap g of the capacitors. These boundary conditions give rise to resonant modes at $\omega_n/2\pi = n\omega_0/2\pi$, $n \in \mathbb{N}$, where $\omega_0 = \pi\bar{c}/l_r$ denotes the fundamental resonance frequency. Here, \bar{c} is the phase velocity of electromagnetic waves in the coaxial cable and l_r the length of the resonator. The joint is located at the center of the resonator, and therefore couples differently to odd and even modes owing to the current nodes and anti-nodes in the mode profiles, as shown in Fig. 11(e). Before investigating the cables with joints, we measure the losses of a bare superconducting cable purchased from KEYCOM Corp. [50] for comparison. The coaxial cable has an outer diameter of 2.19 mm, inner conductor diameter of 0.51 mm and dielectric diameter of 1.62 mm. Both the inner conductor and shield are fabricated from NbTi, the dielectric is fabricated from PTFE. The measurements are carried out in a ^4He bath cryostat at temperatures of 1.6 K and 4 K using a vector network analyzer [Fig. 11(a)]. The temperature is controlled by pumping on the liquid helium in the cryostat. The resonator is connected to a room temperature setup with coaxial cables. The applied microwave power is typically on the order of -30 dBm at the input of the resonator. Since the environmental temperature corresponds to frequencies above 30 GHz, most of the loss-relevant two-level fluctuators are expected to be saturated in our measurements, and therefore, do not cause power-dependent losses. The losses in the resonator are caused by finite coupling to the external circuit and internal losses due to dissipative effects. For each mode, the total loss is described by the loaded quality factor

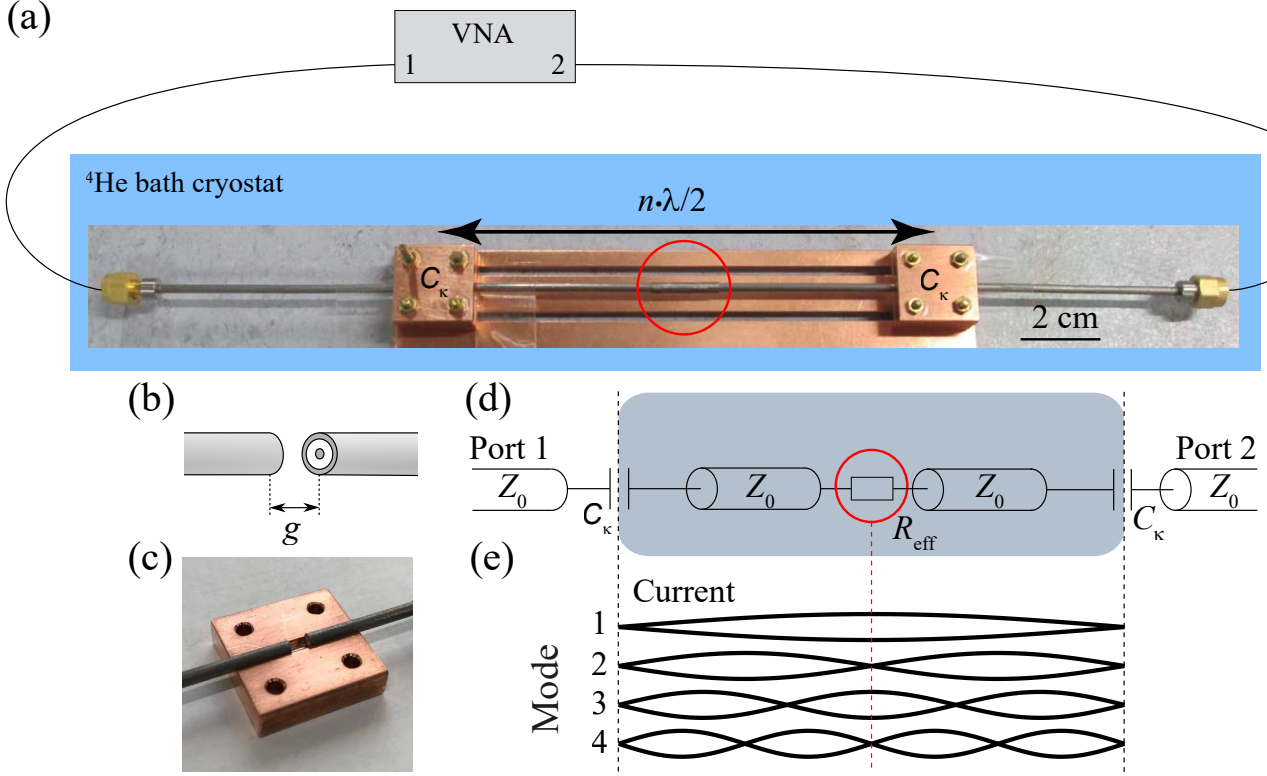


Figure 11. Photographs of the $\lambda/2$ resonator geometry and the corresponding circuit diagram together with current mode profiles. (a) Photograph of the coaxial microwave resonator with a joint in the center (marked by the red circle). Corresponding measurements are carried out using a vector network analyzer (VNA) with the sample immersed in liquid helium. (b) Schematics of the coupling capacitances with gap g . (c) Photograph of an open coupling capacitor. (d) Circuit diagram of the sample. The joint is modelled by an effective resistance R_{eff} . The latter divides the transmission line resonator with a characteristic impedance Z_0 into two parts of equal length with a characteristic impedance Z_0 . The coupling capacitances, C_κ , are nominally identical. (e) Sketch of the current profiles of the four lowest resonant modes. The odd modes have a current antinode and the even modes have a current node at the joint location.

$Q_L = (Q_{\text{int}}^{-1} + Q_{\text{ext}}^{-1})^{-1}$, where Q_{int} represents the internal losses and Q_{ext} represents the external losses. The average lifetime of a microwave photon for mode n in the resonator before being lost by internal dissipative processes is given by $T = Q_{\text{int}}/\omega_n$ and an associated characteristic exponential decay length is $\ell_d = \bar{c}T = \bar{c}Q_{\text{int}}/\omega_n$. Evidently, we can precisely determine the decay length and, thus, losses due to the joint, by measuring the internal quality factor of the resonator. From the input-output formalism, we obtain

$$\frac{|S_{21}^{\text{max}}|}{|S_{11}^{\text{min}}|} = \frac{Q_{\text{int}}}{Q_{\text{ext}}}, \quad (9)$$

where $|S_{21}^{\text{max}}|$ is the maximum of the transmission amplitude peak at the resonance, and $|S_{11}^{\text{min}}|$ is the minimum of the reflection amplitude dip in linear units. To quantify the losses per cable length, we extract the attenuation coefficient α from Q_{int} via the relation [66]

$$Q_{\text{int},n} = \omega_n \frac{Z_0 C_l}{2\alpha_n} = \frac{n\pi}{2\alpha_n l_r}, \quad (10)$$

where $C_l = 88.4 \text{ pF m}^{-1}$ is the capacitance of the coaxial cable per unit length obtained from a finite-element simulation and $Z_0 = 50 \Omega$ is the nominal characteristic impedance. Here, α_n is in units of $1/\text{m}$, and in order to present α_n in units of dB/m , one needs to multiply it with $20/\ln 10 \simeq 8.69$. Furthermore, the decay length can be calculated as $\ell_d = 1/(2\alpha_n)$. We obtain the coupling capacitance C_κ by fitting [66]

$$Q_{\text{ext},n} = \frac{C_l l (1 + \omega_n^2 C_\kappa^2 Z_0^2)}{4\omega_n C_\kappa^2 Z_0} \quad (11)$$

to the extracted Q_{ext} for each mode of the $\lambda/2$ resonator. To characterize the losses in the joint, we use the circuit model depicted in Fig. 11(d). In particular, we model the joint as an effective lumped-element resistor R_{eff} . For the bare resonator without the joint, we set $R_{\text{eff}} = 0$. We apply the ABCD matrix method [67, 68], where the transmission matrix for the resonator with R_{eff} at the center of the resonator is given by

$$\begin{pmatrix} A & B \\ C & D \end{pmatrix} = M_1 M_2 M_3 M_2 M_1, \quad (12)$$

Table II. Main parameters of the bare resonator and the resonators with the connecting joints. The parameters are the resonator length l_r , fundamental frequency $\omega_0/2\pi$, and internal quality factor Q_{int} . The quantity $\alpha_{2\text{ GHz}}$ ($\alpha_{6\text{ GHz}}$) corresponds to the effective attenuation coefficient at 2 GHz (6 GHz) for a microwave transmission line with joints spaced equidistantly at 2 m intervals and is estimated from our measurement results for a single joint. Similarly, the decay length ℓ_d is also shown. The parameters correspond to the temperature of 1.6 K.

Parameter	Unit	Bare cable	With joint
l_r	mm	81	107
$\omega_0/2\pi$	GHz	1.40	1.09
$Q_{\text{int},1}$		1.2×10^6	2.1×10^4
$\alpha_{2\text{ GHz}}$	dB/km	0.2	0.5
$\alpha_{6\text{ GHz}}$	dB/km	0.8	2.0
$\ell_{d,2\text{ GHz}}$	km	25	9.0
$\ell_{d,6\text{ GHz}}$	km	5.5	2.2

with the matrices for the circuit components given by [67]

$$\mathbf{M}_1 = \begin{pmatrix} 1 & \frac{1}{i\omega_n C_\kappa} \\ 0 & 1 \end{pmatrix}, \quad (13)$$

$$\mathbf{M}_2 = \begin{pmatrix} \cosh(\gamma l_r/2) & Z_0 \sinh(\gamma l_r/2) \\ \frac{1}{Z_0} \sinh(\gamma l_r/2) & \cosh(\gamma l_r/2) \end{pmatrix}, \quad (14)$$

$$\mathbf{M}_3 = \begin{pmatrix} 1 & R_{\text{eff}} \\ 0 & 1 \end{pmatrix}. \quad (15)$$

Here, $\gamma = \alpha + i\beta$ is the complex wave propagation coefficient, α is the attenuation coefficient discussed above, and $\beta = \omega/\bar{c}$, where the velocity can be calculated as $\bar{c} = 1/(Z_0 C_l)$. The reflection and transmission coefficients can be obtained from the matrix coefficients as [67]

$$S_{11} = \frac{A + B/Z_0 - CZ_0 - D}{A + B/Z_0 + CZ_0 + D}, \quad (16)$$

$$S_{21} = \frac{2}{A + B/Z_0 + CZ_0 + D}. \quad (17)$$

By using the ABCD method, we can also extract the transmission coefficient of the joint without the resonator determined by the coupling capacitances. Here, we consider a network consisting of only the effective resistor that is connected to input and output lines, and therefore, the ABCD matrix equals to \mathbf{M}_3 given in Eq. (15). The analysis of the joints can be summarized as follows: First, we extract Q_{int} for several modes of the bare resonator, and consequently, we obtain α over a broad frequency range. Then, we measure the quality factors of the resonators with the joints and extract R_{eff} describing the joint using the fact that the cable outside the joint is essentially identical to the cable in the bare resonator. Finally, from R_{eff} we obtain the losses caused by the joint. From the extracted attenuation coefficient of the joint, we estimate numbers for the losses per kilometer for our superconducting transmission line, where joints are placed at two-meter intervals. The resulting

attenuation coefficients for the transmission line are summarized in Table II for frequencies of 2 GHz ($\alpha_{2\text{ GHz}}$) and 6 GHz ($\alpha_{6\text{ GHz}}$). The latter is the relevant value for our experiments. The extracted value of α exceeds the corresponding value of 0.2 dB km^{-1} for optical fiber at telecom frequencies by one order of magnitude [69].

D. System operation and performance

Next, we investigate the cooldown procedure as well as the performance of our cryogenic link. We compare the four different types of cooldown, listed in Tab. III. The first type (CD 1) has been performed prior to the exchange of Alice's Cryomech PT410 with a PT420 model. The second type (CD 2) corresponds to a cooldown with Alice only, after replacing the PT410 PTR with a PT420 model. The third cooldown category (CD 3) for the cryogenic link has been performed after installation of Alice's PT420 and the fourth cooldown type (CD 4) corresponds to a repetition of CD 3 after optimizing for heat leaks between respective cryostat shields. After a full assembly of the system and pumping the OVC to a reasonable vacuum ($\sim 1 \times 10^{-3}$ mbar), we first start the PTRs of Alice, Eve, and Bob simultaneously. Eve and Bob are operated like conventional Oxford Instruments Triton cryostats. For precooling, Bob uses its $^3\text{He}/^4\text{He}$ mixture, and Eve contains a closed precooling circuit, based on ^4He and cryogenic sorption pump heat switches [26]. Alice is pre-cooled manually via a separate ^4He circuit operated with pressures up to $\simeq 4$ bar. The overall precooling procedure takes approximately three days. Figure 12 shows Alice's PTR temperatures during precooling for each respective cooldown, listed in Tab. III, where panel (a) [(b)] corresponds to the PT1 [PT2] stage. The sudden jumps in temperature correspond to a manual adjustment of the precooling pressure and the insets show the respective final steady-state temperature. Within our first cooldown of the entire cryogenic link with the PT410 PTR in Alice (CD 1), we reach a PT2 temperature of 6 K, which is too high to sustain $^3\text{He}/^4\text{He}$ condensation. After upgrading Alice with a PT420 (CD 3), we reach a steady-state temperature of 59 K (4.6 K) on the PT1 (PT2) stage. Despite significant improvement in comparison to operation with the PT410, the final PT2 temperature still exceeds the threshold for helium liquefaction in this case. As a result, in case of CD 3, Alice's dilution circuit could only be operated with strongly reduced cooling power (or: helium throughput). It was found that some care needs to be taken to avoid any touches between respective temperature stages, particularly around the aforementioned copper braids thermally shorting the stainless-steel bellows, visible in Fig. 7. In addition, the impact of thermal radiation from the room temperature stage could be significantly lowered by covering these stainless steel bellows at the PT1 stage with additional Mylar superinsulation. Following these modifications, the heat load is eventually sufficiently low to allow for stable circula-

Table III. Different cooldown categories for Alice. CD 2 describes a cooldown for Alice without the cryogenic link attached.

List of cooldown categories		
Category	Alice cold head	comment
CD 1	PT410	no optimization
CD 2	PT420	Alice only
CD 3	PT420	no optimization
CD 4	PT420	optimized regarding heat leaks

tion of the $^3\text{He}/^4\text{He}$ mixture. Cooldowns following these adaptations fall into category CD 4 and we observe that in the scenario shown in Fig. 12 we reach a steady-state temperature of 49 K (3.6 K) for PT1 (PT2). From the steady-state temperatures in Fig. 12, we observe that the final PT1 temperature is determined by the thermal leak to the OVC shield at the link adapter, whereas the final PT2 temperature is determined by the cooling power, provided by the cold head. Following the precooling procedure, we start the helium condensation as well as dilution cooling. We keep Alice in idle mode and wait for Bob to start with JT cooling, according to the conventional Triton protocol. Thereby, Bob has sufficient cooling power to cool Alice's MC to $\simeq 500$ mK over the link. After Bob has cooled Alice below $\simeq 4$ K, we subsequently start Alice's 1 K circulation and condense the $^3\text{He}/^4\text{He}$ mixture on Alice's side, which typically takes 6 h. Alice's condensation is effectively supported by the Bob cryostat. The overall cooldown procedure takes about 80 h, as shown in Fig. 12.

System operation and performance Figure 13(a) shows the final temperature profile of the MC section of the cryogenic link for CD 1, CD 3 and CD 4. In case of CD 1, the cooling power, provided by the PTR, is insufficient to sustain Alice's $^3\text{He}/^4\text{He}$ condensation cycle. In this case, Bob manages to hold Alice's MC at a steady temperature of 506 mK over the 6 m long MC tube. For CD 3, we can achieve a stable $^3\text{He}/^4\text{He}$ circulation, but only via Alice's scrolls backing pump, not by the TMP itself, which leads to a significant reduction in cooling power. In this case, we reach a final temperature of 111 mK on Alice's side. By reducing the heat leaks at the link adapters prior to CD 4, we can operate Alice with the TMP, leading to a minimal MC temperature of 35 mK with a suitable still heater configuration. We reach a minimal temperature of 52 mK in the center of the MC tube, below Eve. However, to stabilize the condensation pressures, we usually operate Alice without a still heater, leading to a steady temperature of approximately 50 mK for Alice and a center temperature of 55 mK. Next, we investigate heat transfer over the system by varying the center temperature T_{center} of the superconducting transmission line. Such a type of investigation is of crucial relevance in case we employ our system to artificially generate thermal channels in future quantum communication experiments. Measured equilibrium temperatures of Alice's MC, Bob's MC, and Alice's sample stage as a function of T_{center} are plotted in Fig. 13(b). We observe that the MC temperatures of Alice and Bob, as well as

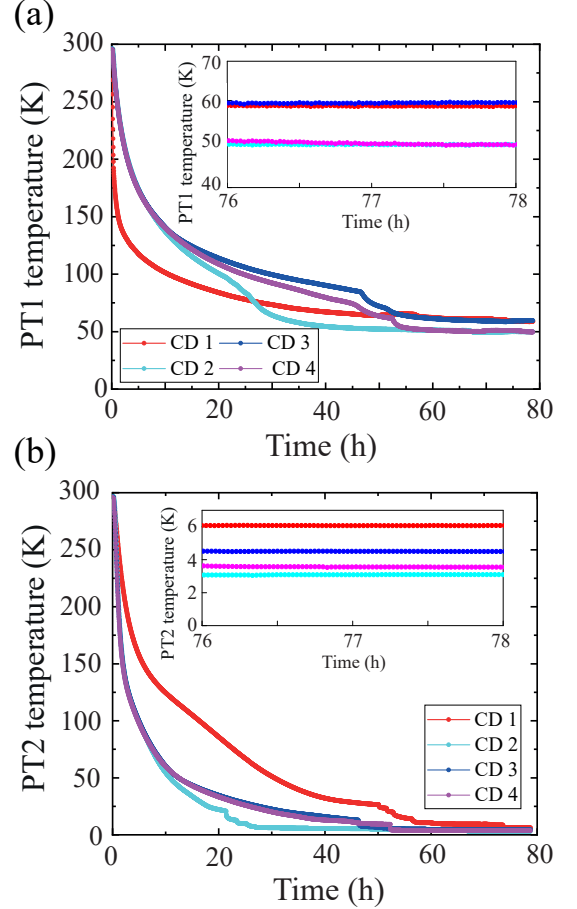


Figure 12. (a) Alice PT1 temperature for the cryogenic link cooldown with the PT410 cold head (red), PT420 cold head (blue) and PT420 cold head after removing thermal leaks (magenta). The cyan line shows the respective data from the Alice test cooldown with the PT420 cold head. The inset shows the steady-state temperatures, reached after approximately 3 days of precooling. (b) Respective results for the Alice PT2 plate.

the temperature of the MC tube below Eve, show an approximately linear increase as a function of T_{center} . As a result, thermal conduction is the dominant source of heat transfer in this case. We explain the deviation from linearity for the Eve MC tube by the comparably strong temperature dependence of thermal conductivity of PEEK [57]. To realize a stable thermal background for quantum experiments, we stabilize our sample stage in Alice to 70 mK for the measurement shown in Fig. 13(b). We choose a slightly higher value compared to MC base

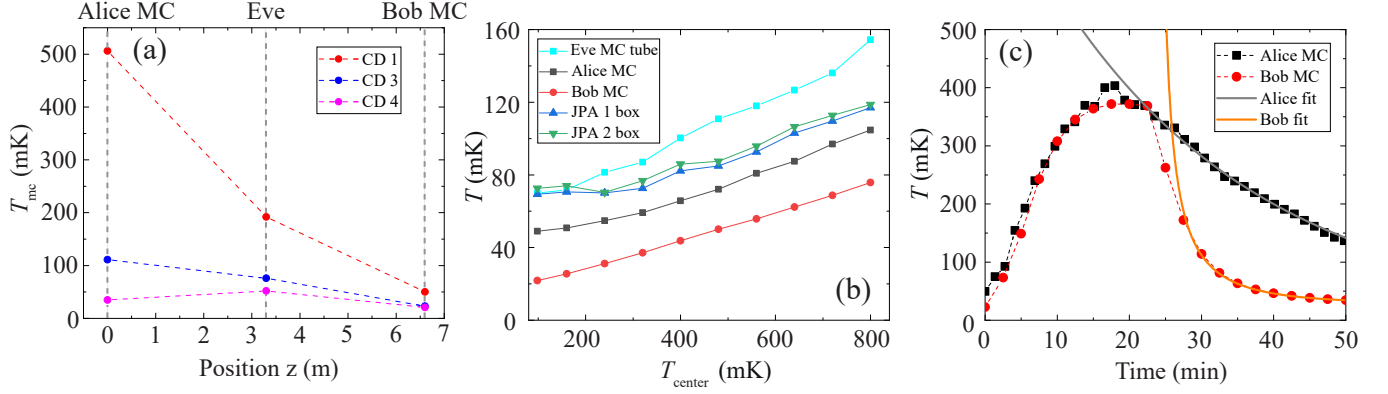


Figure 13. (a) Gradient of the MC tube temperature T_{mc} along the cryogenic link. In case of CD 1, it is not possible to operate the dilution cycle of Alice. For CD 3, Alice relies only on the scrolls backing pump, leading to a significantly reduced cooling power. (b) Effect of PID stabilization of the center temperature T_{center} of our transmission line on the temperature T of the MC tube, the respective MC stage of Alice and Bob, as well as on the sample stage in Alice. We observe an approximately linear increase of the steady-state temperatures, implying that heat transfer is dominated by the thermal conductance of the MC tube. (c) Stress test for the cryogenic link. We stabilize the center at $T_{center} = 4$ K and find that helium condensation of Alice breaks down after 20 min. For temperatures above 100 mK, relaxation to equilibrium can be modelled by an exponent (Alice). For $T \lesssim 100$ mK, we need to take the temperature dependence of the MC cooling power into account (Bob). Solid and dashed lines connecting data points are a guide to the eye.

temperature, to achieve robustness towards temperature fluctuations in the cryogenic link. As can be seen in Fig. 13(b), the sample stage temperature is independent of the center temperature up to $T_{center} \simeq 300$ mK. Since for microwaves, this noise temperature already corresponds to the linear Johnson-Nyquist regime, we can use the cryogenic link to verify the influence of local heating in a superconducting environment. Figure 13(c) corresponds to a stress test of the cryogenic link. During this test, we investigate for how long we can stabilize the center temperature at $T_{center} = 4$ K, such that the cryogenic link effectively forms a thermal channel resembling a liquid helium bath. We find that over the time of approximately 20 min, the MC stages in Alice and Bob heat up to 380 mK. Following that, the heater needs to be switched off since the condensation pressure for Alice's 1 K circuit as well as for the $^3\text{He}/^4\text{He}$ circuit have reached critical values. Bob relaxes back to equilibrium within 30 min, whereas Alice cools down significantly slower. This finding indicates that our system is asymmetric regarding its cooling power. In contrast, Alice and Bob show similar behavior during warm-up, implying that the cryogenic link is symmetric with respect to its thermal conductivity and heat capacity. As can be seen in Fig. 13(c), we fit the cooling curves of Alice and Bob. Alice's curve can be accurately fitted by an exponential Newton-like cooling law. For Bob, we fit the asymptotic cooldown for temperatures below 100 mK, where we take the quadratic temperature dependence of the MC cooling power into account [51, 70].

Next, we investigate the temperature profile along our superconducting transmission line. To enable photon number calibration over the cryogenic link via Planck

spectroscopy [32], the transmission line is connected to heatable attenuators on the Alice side. During the first successful cooldown of category CD 4, we measure a steady-state attenuator temperature of $T_a = 102$ mK and corresponding $T_{center} = 121$ mK. Since these temperatures significantly exceed the MC temperature, we increase the thermal coupling of the attenuator to the MC plate before the subsequent cooldown, leading to a reduction of the attenuator temperature $T_a = 46$ mK. Following this modification, the temperature of the cable in the center reaches the steady value $T_{center} = 110$ mK. In general, the measured center temperature reaches its minimum shortly after cooldown, before we switch on our microwave devices, and our lowest recorded temperature corresponds to $T_{center} = 97.4$ mK. These comparably high values of T_a and T_{center} indicate a significant level of thermal radiation inside the MC shields. The high attenuator temperature can be explained by the fact that the heatable 30 dB attenuator is well approximated by a black body radiator, whereas the copper MC shields are highly reflective, implying that the heatable attenuators form dominant heat sinks. To determine the temperature profile $T(z)$ along the transmission line, we treat the transmission line as a quasi-1D object with length l . In addition, we assume that the thermal coupling to the MC is dominated by the silver wires with thermal conductivity λ_{Ag} and cumulative cross section A_{Ag} . We find the steady-state heat equation

$$-\lambda_{Ag} A_{Ag} \frac{\partial^2 T}{\partial z^2} = \dot{Q}_c + \dot{Q}_r + \dot{Q}_h, \quad (18)$$

where \dot{Q}_c denotes conductive heat transfer between the MC tube and the transmission line, mediated by the PEEK holders, \dot{Q}_r corresponds to the radiative heat load

and the contribution \dot{Q}_h describes local heating. We solve Eq. (18) using a finite-difference method. The corresponding results are plotted in Fig. 14, where we take Alice's heatable attenuator temperature and Bob's MC temperature as Dirichlet boundary conditions. Stars correspond to the measured temperature values. We determine $\dot{Q}_r = 0.52 \mu\text{W}$ such that the orange curve matches the experimental center temperature. For increased thermal coupling of the attenuators, Eq. (18) predicts a center temperature of $T_{\text{center}} = 111.9 \text{ mK}$, which is close to the measured value of 110 mK . A possible origin for an additional radiation leak into the MC shield is the fact that the MC tube consists of two separate segments, which are plugged into each other and connected with annealed silver. This purely mechanical connection provides flexibility regarding the tube length, but does introduce the possibility of a small gap at the connection point. Assumptions of the 'worst case' gap leading to additional 1 K radiation impinging on the microwave link do not seem consistent with the $0.52 \mu\text{W}$ heat load determined above. However, in future experiments, the impact of radiative heat load can be reduced by covering the inside of the MC shields with SiC-based absorption coating [71] or by inserting additional black absorbers into the orifices of the link adapters.

Heat transport over the cryogenic link We treat the transmission line as quasi-1D object, extending from $z = -l/2$ to $z = l/2$, where l denotes the length of the cryogenic link. In addition, we assume that thermal coupling to the MC is dominated by the silver wires with thermal conductivity λ_{Ag} and cumulative cross section A_{Ag} . Regarding the respective thermal conductivity of the involved components, we perform the approximations described in Appendix B. The steady-state heat equation is then given by Eq. (18). The first source term describes conductive heat transfer between the MC tube and the transmission line,

$$\dot{Q}_c = \sum_{n=-(N-1)/2}^{(N-1)/2} \dot{q}[T(z)] \delta\left(z - \frac{nl}{N-1}\right). \quad (19)$$

In Eq. (19), we model the thermal coupling of the N PEEK support holders to the MC tube by a finite Dirac-comb due to their tip-shaped geometry [cf. Fig. 10(a)]. The heat $\dot{q}[T(z)]$ that flows over each support holder depends on the solution $T(z)$ and is modelled by

$$\dot{q}[T(z)] = \lambda_P[T(z)] \frac{A_P}{h_P} [T_{\text{tube}} - T(z)], \quad (20)$$

where T_{tube} corresponds to the temperature of the MC tube, A_P (h_P) denotes the respective effective cross section (height) of the PEEK support holders, and the thermal conductivity $\lambda_P[T(z)]$ follows the temperature dependence given by Eq. (5). The radiative source term in Eq. (18) is modelled by [72]

$$\dot{Q}_r = \frac{\sigma[T_r^4 - T^4(z)]}{\left(\frac{1-\varepsilon_r}{A_r \varepsilon_r}\right) + \left(\frac{1-\varepsilon_t}{A_t \varepsilon_t}\right) + \frac{1}{A_r F_{r \rightarrow t}(z)}}, \quad (21)$$

where the quantities A_r (A_t) and ε_r (ε_t) denote the respective area and integral emissivity associated with the radiation leak, T_r is the effective temperature of the radiation leak (transmission line), $F_{r \rightarrow t}(z)$ corresponds to the position-dependent view factor between the transmission line and the radiation leak, and $\sigma = 5.67 \times 10^{-8} \text{ W m}^{-2} \text{ K}^{-4}$ is the Stefan-Boltzmann constant. The third source term

$$\dot{Q}_h = P_h \delta(z) \quad (22)$$

models local heating in the center, $z = 0$, with power P_h . The boundary conditions for Eq. (18) are determined by the cooling power \dot{Q}_{mc} of Alice and Bob at the MC stage, which can be expressed as [51, 70, 73, 74]

$$\dot{Q}_{\text{mc}} = 84 \dot{n}_3 T_{\text{mc}}^2 \left(\frac{\text{J}}{\text{mol} \cdot \text{K}^2} \right) \quad (23)$$

for temperatures $T_{\text{mc}} \lesssim 100 \text{ mK}$ in case of efficient pre-cooling of the inflowing ^3He . The quantity \dot{n}_3 corresponds to the ^3He circulation rate and T_{mc} denotes the MC temperature. Consequently, since T_{mc} depends on $T(z)$, the boundary conditions are solution-dependent. Resulting from this fact, as well as from the nonlinearity of the source terms, we make three approximations to simplify Eq. (18), which enables a solution using a simple finite-difference method. In the approximation, we assume the radiative heat load to be equally distributed, implying $F_{r \rightarrow t}(z) \simeq \text{const.}$ and $\dot{Q}_r \simeq \langle \dot{Q}_r \rangle$, where $\langle \dots \rangle$ implies an average over the temperature profile of the cable. The effect of this approximation is small since radiation, emitted by the transmission line, anyway can be neglected due to the low temperature of the cable, $T(z)^4 \ll T_r^4$. Consequently, we treat radiation as a constant source term. In the second approximation, we replace the temperature-dependent thermal conductivity of PEEK with an average value, $\lambda_P[T(z)] = \lambda_P[\langle T(z) \rangle]$. We update this average in an iterative approach and repeat the numerical routine for M times, where we determine the averages $\langle \dots \rangle$ for iteration step j from the solution in step $j-1$. We repeat the procedure until we converge, which is sufficient for $M = 50$ in our case. The third approximation is related to the boundary conditions. As mentioned above, Eq. (20) needs to be solved for fixed MC cooling power, which depends on the solution itself. For our numerical solution, we approximate these boundary conditions with Dirichlet-conditions, implying that we fix the temperature at the boundaries. This approximation is also necessary since we do not know the exact relation between T_{mc} , $T(-l/2)$ and $T(l/2)$. To estimate the error made by this third approximation, we compare our numerical solution to a special case where the heat equation can be solved analytically. This case corresponds to the dependence of the temperature $T_{\text{center}} = T(0)$ on local heating of the center with specific power $p = P_h/A_{\text{Ag}}$ under the assumption of perfect isolation, apart from direct thermalization to the MC stage. We assume constant temperature T_0 in a domain $-\infty < z < \infty$ prior to switching on the heating at

time $t = 0$. Regardless of the functional shape on $T(z)$, the respective cooling power \dot{q} of Alice and Bob, assumed to be located at $z = -l/2$ and $z = l/2$, adjusts in a way that the global energy balance between sources and sinks is satisfied in steady state, $p = -2\dot{q}$. As a result, we can rewrite the time-dependent heat equation without any boundary conditions as

$$\frac{\partial T}{\partial t} - \kappa \frac{\partial^2 T}{\partial z^2} = -\frac{p}{2\rho c} [\delta(z-l/2) + \delta(z+l/2)] + \frac{p}{\rho c} \delta(z), \quad (24)$$

where $\kappa \equiv \lambda_{\text{Ag}}/(\rho c)$, with the density ρ and specific heat c of the transmission line, assumed to be dominated by the silver. We assume that prior to switching on the heater at $t = 0$, the system is in thermal equilibrium at $T = T_0$. The solution can then be determined via the Green's-function [75]

$$G(z, t) = \frac{1}{\sqrt{4\pi\kappa t}} e^{-\frac{z^2}{4\kappa t}} \quad (25)$$

to be

$$T_{\text{center}}(t) = T_0 + \frac{p}{\rho c} \int_0^t ds [G(0, s) - G(l/2, s)].$$

The steady-state solution can then be expressed as

$$\lim_{t \rightarrow \infty} T_{\text{center}}(t) = T_0 + \frac{P_h l}{4\lambda_{\text{Ag}} A_{\text{Ag}}}. \quad (26)$$

The factor of 4 arises from the assumed symmetry of the system: half of the heater power respectively flows along half of the link length. This result can be directly compared to the center temperature obtained with our numerical routine for this specific scenario. We determine typical deviations of 1 – 2 %, which we attribute to

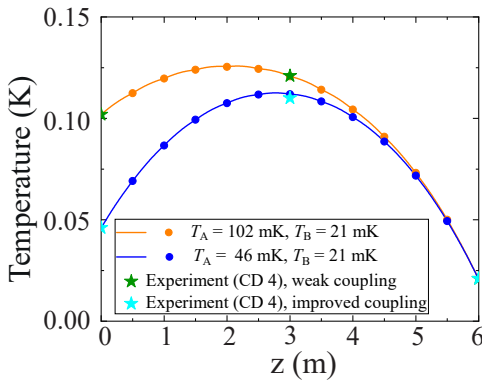


Figure 14. Temperature profile along the transmission line for different thermal coupling of the heatable attenuators on Alice's side. Stars correspond to measured temperatures. Solid lines are the result of a heat equation simulation which takes thermal conductivity as well as radiation into account. As Dirichlet boundary conditions, we employ the recorded heatable attenuator temperature for Alice and the MC temperature for Bob.

the approximation error of the global energy balance by Dirichlet boundary conditions. The solutions, depicted by the solid lines in Fig. 14, are numerically obtained from Eq. (18) by dividing the transmission line into 600 discrete segments. For the thermal conductivities, we use the values from Appendix B. In addition, we use $A_{\text{Ag}} = 0.035 \text{ cm}^2$, $h_{\text{P}} = 1 \text{ cm}$ and $A_{\text{P}} = 0.72 \text{ cm}^2$. We use the temperature of the heatable attenuators in Alice's and Bob's MC temperature as Dirichlet boundary conditions. Matching to the experimentally determined center temperature of the transmission line is then found for $\langle \dot{Q}_{\text{r}} \rangle \simeq 0.52 \text{ } \mu\text{W}$. This additional heat leak cannot currently be entirely accounted for, but future work is planned to investigate potential sources of unwanted radiation.

Fit function for relaxation of the MC stage In the following, we provide more details about the fits of the cooldown of the MC in Alice and Bob, depicted by the solid lines in Fig. 13(c). For Alice, the temperature range from $T_0 = 369 \text{ mK}$ to 136.8 mK can be well fitted by an exponential law, $T(t) = T_0 e^{-bt}$, where b is treated as a fit parameter. As a consequence, in this elevated temperature regime, the cooling power does not follow the quadratic temperature dependence Eq. (23), and the temperature decreases in a Newton-like behavior. For Bob, we fit the temperature range below $T_0 = 114 \text{ mK}$. Cooling in this temperature regime is predicted to be described by Eq. (23), resulting from successive reduction of the cooling power for temperatures approaching 0 K. In addition, we assume that heat leaks are dominated by thermal conductance. Consequently, the temperature of Bob's MC satisfies

$$\frac{dT}{dt} = g[T_e - T(t)] - aT(t)^2, \quad (27)$$

where T_e corresponds to an effective environmental temperature, associated with the heat leak, and a and g are constants. By defining the auxiliary function $h(x) = x + g/(2a)$, the solution of this Riccati type equation [56] can be expressed as

$$T(t) = h(T_*) \left[\frac{h(T_0) + h(T_*) \tanh[a \cdot t \cdot h(T_*)]}{h(T_*) + h(T_0) \tanh[a \cdot t \cdot h(T_*)]} - 1 \right] + T_*, \quad (28)$$

where T_* denotes the steady-state temperature and $T_0 = T(0)$. To fit Bob's cooldown curve in Fig. 13(c), we fix $T_* = 29.7 \text{ mK}$ and $T_0 = 114.1 \text{ mK}$ and treat a and g as fit parameters. We observe that the asymptotic cooldown behavior of Bob follows Eq. (28).

Lifetime limitation of the cryogenic link For the experiments described in this paper, a typical duration of a single cool down of the cryogenic link has been limited to approximately three weeks. This time constraint is determined by the performance of the home-built cryostat since Alice was found to be more sensitive to the temperatures attained at the various fridge stages. During operation, we have observed consecutive loss of cooling power at the PT1 and PT2 stages, manifesting as a

slow and steady temperature uptrend. The corresponding PT1 temperature for three different cooldowns of category CD 4 is plotted in Fig. 15(a). We observe that for cooldowns in April and March, the slopes for the temperature uptrend approximately coincide. The offset between both curves results from the fact that we have added Mylar superinsulation foil to multiple specific uncovered locations at the PT1 stage between both cooldowns. We find that the slope is significantly higher for the cooldown in July. A similar temperature uptrend is measured for the PT1 stages of Bob and Eve. After three weeks, the cooling power is no longer sufficient to operate Alice's dry 1 K pot, which is necessary to guarantee efficient precooling of the inflowing ^3He . In contrast to Alice, the temperature uptrend did not lead to a detectable reduction of Bob's cooling capacity. In Fig. 15(b), we plot the measured PT1 temperature for Alice in case of evacuated helium cycles (apart from the PTR) in the system. Consequently, this temperature uptrend cannot result from cold leaks or dirt in the $^3\text{He}/^4\text{He}$ system. After three weeks of operation, we find a gas accumulation of 0.7 mbar in the OVC volume at room temperature.

In the following, we investigate the hypothesis that this gas consists mainly of water vapor which is either a result from trapped moisture in the superinsulation foil or from diffusion through the Viton O-rings [76]. In a rough approximation, we assume that this water forms a layer of ice on top of the PT1 shield and thereby slowly forms a film with emissivity

$$\varepsilon_f(t) = (1 - e^{-kt})\varepsilon_* + e^{-kt}\varepsilon_s, \quad (29)$$

where ε_s denotes the emissivity of our Mylar superinsulation, ε_* is the emissivity of ice, k denotes the ice formation rate, and t is time. Since bulk ice can be approximated as a black body at infrared wavelengths, Eq. (29) leads to a significant change of the radiative heat balance. As a result of Eq. (29), the effective cooling power at the PTR stages decreases successively during operation of the cryogenic link as a change of reflection properties significantly affects the heat balance of the system. This change of the heat balance leads to a slow uptrend of the PT1 and PT2 temperatures. The net heat flow between two gray bodies with temperatures T_1, T_2 , areas A_1, A_2 , emissivities $\varepsilon_1, \varepsilon_2$, and respective view factor $F_{1 \rightarrow 2}$ is given by [72]

$$\dot{Q}_{1 \rightarrow 2} = \frac{\sigma (T_1^4 - T_2^4)}{\left(\frac{1-\varepsilon_1}{A_1\varepsilon_1}\right) + \left(\frac{1-\varepsilon_2}{A_2\varepsilon_2}\right) + \frac{1}{A_1 F_{1 \rightarrow 2}}}. \quad (30)$$

We assume that the shields are close to each other, and that radiation is distributed homogeneously, implying that we use the approximation of equal areas, $A_1 \simeq A_2$, and ideal view factor $F_{1 \rightarrow 2} \simeq 1$. First, we consider the ideal situation where no ice film forms, $\varepsilon_f = \varepsilon_s$. In this case, the net heat flux per unit area between the OVC shield and the top layer of the superinsulation foil can be

expressed as

$$\dot{q}_{r \rightarrow s} = \frac{\varepsilon_r \varepsilon_s \sigma}{\varepsilon_r + \varepsilon_s - \varepsilon_r \varepsilon_s} (T_r^4 - T_s^4), \quad (31)$$

where T_r (ε_r) denotes temperature (emissivity) of the OVC aluminum shield, and T_s is the temperature at the top layer of the superinsulation foil. The net heat flux per unit area through the N -layer superinsulation foil is given by [70]

$$\dot{q}_s = \frac{\varepsilon_s \sigma}{N + 1} (T_s^4 - T_0^4), \quad (32)$$

where T_0 denotes the equilibrium PT1 temperature in the ideal scenario without ice. In thermal equilibrium, the heat fluxes in Eq. (31) and Eq. (32) are in balance with the specific cooling power p of the PT1 stage, which we assume to be temperature independent in our model,

$$\dot{q}_{r \rightarrow s} = \dot{q}_s = p. \quad (33)$$

We compare this ideal situation with the scenario where the ice layer forms. In a rough approximation, we assume that the ice film forms on top of the superinsulation foil. In this case, we obtain the net heat flux between the room temperature shield and the ice film

$$\dot{q}_{r \rightarrow f} = \frac{\sigma \varepsilon_r \varepsilon_f(t)}{\varepsilon_r + \varepsilon_f(t) - \varepsilon_r \varepsilon_f(t)} (T_r^4 - T_f(t)^4). \quad (34)$$

The top of the superinsulation foil then has a temperature $T_f(t)$, leading to the specific heat flux

$$\dot{q}_{f \rightarrow \text{PT1}} = \frac{\varepsilon_s \sigma}{N + 1} (T_f(t)^4 - T(t)^4). \quad (35)$$

We assume that the uptrend is sufficiently slow to perform an adiabatic approximation. Consequently, at any time, we can assume the system to be in thermal equilibrium. We then have

$$\dot{q}_{r \rightarrow f} = \dot{q}_{f \rightarrow \text{PT1}} = p. \quad (36)$$

From the conditions Eq. (33) and Eq. (36), we find

$$T(t)^4 + T_s^4 = T_f(t)^4 + T_0^4. \quad (37)$$

In a lengthy but straightforward calculation, we can eliminate T_f , T_s , and p from the heat balance. We then find the relation

$$T(t)^4 = T_r^4 + (T_0^4 - T_r^4)\eta(t), \quad (38)$$

where

$$\eta(t) = 1 - \frac{\varepsilon_r[\varepsilon_f(t) - \varepsilon_s]}{\varepsilon_f(t)[\varepsilon_s + \varepsilon_r(N + 2 - \varepsilon_s)]}. \quad (39)$$

We use Eq. (38) for the fit shown in Fig. 15(b), where we treat the ice formation rate k as the only fit parameter. For the fit, we use $N = 40$, $\varepsilon_r = 0.2$ [77], $\varepsilon_s = 0.05$, $T_r = 298$ K and the experimentally determined PT1 base

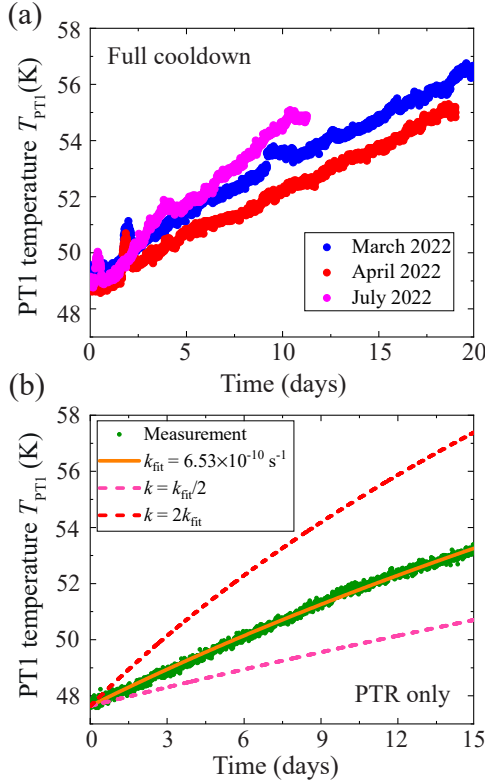


Figure 15. (a) Detected temperature uprends of the PT1 stage for three different cooldowns of category CD4. The corresponding thermometer has been attached on top of Alice's PT1 plate. (b) Experimentally reproduced temperature uptrend in case we only operate the PTRs and keep all helium cycles evacuated (green dots). The orange line corresponds to a fit, based on Eq. (29), where we treat the quantity k as the only fit parameter.

temperature $T_0 = 47.64 \text{ K}$. For the emissivity of ice, we use the bulk value $\varepsilon_* = 0.98$, which is a rough approximation since the actual emissivity of a thin film can be different and most probably changes with film thickness. The solid line in Fig. 15(b) corresponds to a fit according to Eq. (38), where we treat the ice formation rate k as the only fit parameter. Dashed lines show the results, corresponding to $k = k_{fit}/2$ and $k = 2k_{fit}$. We observe that the fit well reproduces the concave time dependence of the temperature uptrend.

An indicator that substantiates the hypothesis that the lifetime of the cryogenic link is limited by ice formation is the fact that we observe the aforementioned gas accumulation of 0.7 mbar in the cryogenic link volume, detected at room temperature after approximately three weeks of cooldown. To investigate the composition of this gas, we connect an external cryogenic pump, cooled by liquid nitrogen to the OVC volume after warm up of the entire system. We observe that the cryopump can adsorb a significant portion of this gas, indicating a major fraction of atmospheric contributions. One possible explanation for the origin of this gas in the OVC volume is outgassing of

the superinsulation foil, e.g., of trapped moisture. A second reason for water accumulation in the OVC volume is diffusion through our Viton O-rings. This hypothesis is based on the significant amount of O-ring seals as well as on the fact that the slope of the temperature uptrend is higher for the cooldown in July, compared to March and April due to the exponential temperature dependence of atmospheric humidity, as predicted by the August-Roche-Magnus equation [78]

$$\varphi_{H_2O} p_v = 0.0061094 \cdot \varphi_{H_2O} \cdot \exp\left(\frac{17.625T[^\circ\text{C}]}{T[^\circ\text{C}] + 243.04}\right) \text{ bar}, \quad (40)$$

where p_v denotes the vapour pressure of water and φ_{H_2O} corresponds to the relative humidity. In the following, we assume $T = 25^\circ\text{C}$ and the average relative humidity of Munich, $\varphi_{H_2O} = 0.67$ [79]. Our system consists of 14 large Viton O-rings (BS389), 26 medium sized O-rings (reference: BS270) and of the order of 50 small O-rings for feedthroughs which can be used for microwave or DC wiring or for helium tubes. The total gas permeation rate through these O-ring seals can be expressed as [80]

$$\dot{V} = \sum_y \sum_x g K_x p_x N_y f_y, \quad (41)$$

where p_x (K_x) labels the partial pressure (permeation coefficient) for gas type x , N_y (f_y) denotes the number of O-rings (form factor) for seal geometry y , and g accounts for lubrication. In Eq. (41), we express f_y in terms of the O-ring diameter D_y , cross-sectional diameter d_y , trench depth h_y , and clearance gap g_y under the assumption of elliptical O-ring distortion

$$f_y = \frac{\pi^2}{2} \frac{D_y + d_y}{d_y^2 \arccos\left(\frac{h_y^2 + g_y^2 + 2h_y g_y}{d_y^2}\right)} \sqrt{d_y^4 - (h_y + g_y)^4}. \quad (42)$$

According to Ref. [80], the permeation rate strongly depends on ambient parameters such as temperature. For our Viton O-rings, permeation is especially high for polar molecules, such as water. In literature, we can find values up to $K_{H_2O} = 216 \times 10^{-8} \text{ sccm s}^{-1} \text{ bar}^{-1} \text{ cm}^{-1}$. We consider permeation of H_2O , N_2 and O_2 and neglect all remaining atmospheric gas contributions due to their low partial pressures. Using the permeation coefficients in Ref. [80], we find

$$\frac{\dot{V}_{N_2}}{\dot{V}_{H_2O}} = 0.119, \quad \frac{\dot{V}_{O_2}}{\dot{V}_{H_2O}} = 0.078. \quad (43)$$

The pressure increase over a time interval Δt is given by

$$\Delta p = \frac{p_{\text{atm}}}{V_l} \dot{V}_{H_2O} \left(1 + \frac{\dot{V}_{N_2}}{\dot{V}_{H_2O}} + \frac{\dot{V}_{O_2}}{\dot{V}_{H_2O}}\right) \Delta t, \quad (44)$$

where V_l denotes the volume of the cryogenic link. Equation (41) predicts a gas accumulation of 1.3 mbar within three weeks [80]. The numerical value of Δp exceeds our

Table IV. Table of characteristic parameters for the JPA, employed for the measurements described in Sec. III. The quantities Q_e (Q_i) denote the the external (internal) quality factor. The given value for Q_i is a conservative lower bound. In addition, we provide the bare resonator frequency ω_r , the critical current I_c , the effective loop inductance L_1 and the Josephson coupling energy E_J .

Q_e	Q_i	$\omega_r/2\pi$ (GHz)	I_c (μ A)	L_1 (pH)	E_J/h (THz)
157 – 215	> 9800	6.00 ± 0.01	4.72 ± 0.03	44.1 ± 0.1	2.35 ± 0.02

detected pressure increase. However, resulting from the corresponding simplifications and uncertainties, we expect our estimation to be reliable regarding the order of magnitude. Nevertheless, this result is a strong indicator that gas accumulation in the OVC mainly results from diffusion of water through the O-rings. Possible long-term solutions for the described problem include an upgrade of the cooling power of Alice and installation of cryogenic vapor traps, or the use of two separated stacked OVC stages with respective individual O-ring seals. For a practical solution, we have upgraded Alice with an additional JT heat exchanger, similar as in Bob, increasing the expected lifetime to multiple months. The diffusion rate from the atmosphere into the OVC is furthermore expected to decrease drastically by replacing the Viton O-rings with metal seals [81].

E. JPA samples and experimental setup

The JPA, employed for the measurements described in Sec. III, has been manufactured at VTT Technical Research Centre of Finland Ltd. The niobium resonator as well as the niobium dc-SQUID with loop area $3.9 \times 3.9 \mu\text{m}^2$ are patterned onto a $675 \mu\text{m}$ thick silicon wafer. A table of characteristic parameters for this type of JPA is provided in Tab. IV. The external (internal) quality factor Q_e (Q_i) are measured by probing the resonator in reflection using a Rohde & Schwarz ZNA26 vector network analyzer (VNA). The bare resonator frequency $\omega_r/2\pi$, the critical current I_c , as well as the loop inductance L_1 , are determined by fitting the tunable JPA resonance frequency as a function of DC flux bias. The DC flux bias is generated by biasing a custom made superconducting coil using a Keithley SourceMeter 240. The Josephson coupling energy E_J is determined by analyzing the nonlinear response. The JPA sample temperature is thermally stabilized to 60 mK via a PID control architecture, implemented with a Picowatt AVS-47 resistance bridge and a 100Ω heater, to guarantee steady squeezing and noise properties. For microwave pumping of the JPA, we use a Rohde & Schwarz SGS100A microwave source. We modulate the pump signal using a data timing generator (DTG) [19, 30, 33, 36]. During the first pulse, we switch off the pump source to obtain a reference for quantum state reconstruction and during a second pulse we switch on the pump. For photon number calibration in our system, we employ Planck spectroscopy [32]. We vary the temperature of a heatable 30 dB attenuator in the JPA input line within the temperature range of 60 mK – 500 mK. This heatable attenuator can

be approximated by a black-body radiator and acts as a self-calibrated cryogenic photon source. This enables us to directly map the detected voltage in the output signals to the photon number in the cryogenic quantum signal [32]. We reconstruct our squeezed states at a frequency of $\omega_0/2\pi = 5.65$ GHz. Consequently, we choose the pump frequency to be $\omega_p = 2\omega_0$, where the phase of the pump is stabilized via a phase-locked feedback loop. The resulting squeezed state is symmetrically split via a Miteq CPL-5850-100B hybrid ring. One of the output modes is kept locally at Alice’s side, and the second output mode is transmitted over the cryogenic link. Both modes undergo multiple amplification stages consisting of a respective cryogenic high-electron-mobility transistor (HEMT) amplifier in the Alice and Bob cryostats and additional room temperature amplifiers, which are stabilized in temperature by a Peltier cooler. As the first segment in the amplification chain, the HEMT amplifiers determine the overall amplification noise due to their high gain ($G_H \simeq 40$ dB). After amplification, the respective signal in both output paths is downconverted to an intermediate frequency (IF) of 11 MHz in a heterodyne detection setup, located in Alice lab, using a local oscillator (LO). This heterodyne microwave receiver setup is extensively described in Refs. [18, 19, 33, 34, 38, 41, 82]. The downconverted IF-signal is then digitized by a National Instruments NI-5782 transceiver module and processed with a National Instruments PXIe-7975R FPGA with a sampling frequency of 125 MHz. The resulting digital signals are downconverted into DC signals and digitally filtered with a finite-impulse response (FIR) filter with single-side bandwidth of 200 kHz. From the filtered data, we determine the 69 two-mode quadrature moments $\langle I_1^n I_2^m Q_1^k Q_2^l \rangle$ with $n + m + k + l \leq 4$ for $n, m, k, l \in \mathbb{N}_0$. For the moment calculation, we average over 9×10^4 time traces with respective trace length 88 μs per pulse before transmitting the moments to a PC for further data processing. Each of these measurements is repeated for 7 times. On the PC, the recorded traces are separated into different parts according to the DTG pulse timings. We reconstruct our bipartite quantum states using a reference-state reconstruction method, where we treat the first pulse as a reference for eliminating the noise moments, added by the amplification chain. In addition, we assume that all reconstructed states are Gaussian, which implies that the corresponding Wigner function is determined by moments up to second order [37]. We employ moments of third and fourth order to determine the cumulants, corresponding to the reconstructed phase-space quasiprobability distribution. Since vanishing cumulants of order larger than two are a necessary and sufficient

criterion for Gaussianity, we employ the cumulants for verifying whether the Gaussian approximation is justified [36]. We synchronize the VNA, the DTG, the FPGA

card, and the LO via a 10 MHz rubidium frequency standard. The microwave pump source is daisy chained to the LO with a 1 GHz reference signal.

-
- [1] H. J. Kimble, “The quantum internet,” *Nature* **453**, 1023–1030 (2008).
 - [2] M. Pompili, S. L. N. Hermans, S. Baier, H. K. C. Beukers, P. C. Humphreys, R. N. Schouten, R. F. L. Vermeulen, M. J. Tiggeleman, L. dos Santos Martins, B. Dirkse, S. Wehner, and R. Hanson, “Realization of a multinode quantum network of remote solid-state qubits,” *Science* **372**, 259–264 (2021).
 - [3] Tim van Leent, Matthias Bock, Florian Fertig, Robert Garthoff, Sebastian Eppelt, Yiru Zhou, Pooja Malik, Matthias Seubert, Tobias Bauer, Wenjamin Rosenfeld, Wei Zhang, Christoph Becher, and Harald Weinfurter, “Entangling single atoms over 33 km telecom fibre,” *Nature* **607**, 69–73 (2022).
 - [4] Sheng-Kai Liao, Wen-Qi Cai, Wei-Yue Liu, Liang Zhang, Yang Li, Ji-Gang Ren, Juan Yin, Qi Shen, Yuan Cao, Zheng-Ping Li, Feng-Zhi Li, Xia-Wei Chen, Li-Hua Sun, Jian-Jun Jia, Jin-Cai Wu, Xiao-Jun Jiang, Jian-Feng Wang, Yong-Mei Huang, Qiang Wang, Yi-Lin Zhou, Lei Deng, Tao Xi, Lu Ma, Tai Hu, Qiang Zhang, Yu-Ao Chen, Nai-Le Liu, Xiang-Bin Wang, Zhen-Cai Zhu, Chao-Yang Lu, Rong Shu, Cheng-Zhi Peng, Jian-Yu Wang, and Jian-Wei Pan, “Satellite-to-ground quantum key distribution,” *Nature* **549**, 43–47 (2017).
 - [5] Frank Arute *et al.*, “Quantum supremacy using a programmable superconducting processor,” *Nature* **574**, 505–510 (2019).
 - [6] V. V. Sivak, A. Eickbusch, B. Royer, S. Singh, I. Tsioutsios, S. Ganjam, A. Miano, B. L. Brock, A. Z. Ding, L. Frunzio, S. M. Girvin, R. J. Schoelkopf, and M. H. Devoret, “Real-time quantum error correction beyond break-even,” *Nature* **616**, 50–55 (2023).
 - [7] Zhongchu Ni, Sai Li, Xiaowei Deng, Yanyan Cai, Libo Zhang, Weiting Wang, Zhen-Biao Yang, Haifeng Yu, Fei Yan, Song Liu, Chang-Ling Zou, Luyan Sun, Shi-Biao Zheng, Yuan Xu, and Dapeng Yu, “Beating the break-even point with a discrete-variable-encoded logical qubit,” *Nature* **616**, 56–60 (2023).
 - [8] Mark Webber, Vincent Elfving, Sebastian Weidt, and Winfried K. Hensinger, “The impact of hardware specifications on reaching quantum advantage in the fault tolerant regime,” *AVS Quantum Science* **4**, 013801 (2022), <https://pubs.aip.org/avs/aqs/article-pdf/doi/10.1116/5.0073075/16493244/013801.1.online.pdf>.
 - [9] Guillermo F. Peñas, Ricardo Puebla, Tomás Ramos, Peter Rabl, and Juan José García-Ripoll, “Universal deterministic quantum operations in microwave quantum links,” *Phys. Rev. Appl.* **17**, 054038 (2022).
 - [10] F. Setiawan, Peter Groszkowski, and Aashish A. Clerk, “Fast and robust geometric two-qubit gates for superconducting qubits and beyond,” *Phys. Rev. Appl.* **19**, 034071 (2023).
 - [11] S. Rosenblum, Y. Y. Gao, P. Reinhold, C. Wang, C. J. Axline, L. Frunzio, S. M. Girvin, Liang Jiang, M. Mirrahimi, M. H. Devoret, and R. J. Schoelkopf, “A cnot gate between multiphoton qubits encoded in two cavities,” *Nature Communications* **9**, 652 (2018).
 - [12] Youpeng Zhong, Hung-Shen Chang, Audrey Bienfait, Étienne Dumur, Ming-Han Chou, Christopher R. Conner, Joel Grebel, Rhys G. Povey, Haoxiong Yan, David I. Schuster, and Andrew N. Cleland, “Deterministic multi-qubit entanglement in a quantum network,” *Nature* **590**, 571–575 (2021).
 - [13] R. Van Meter and S. J. Devitt, “The path to scalable distributed quantum computing,” *Computer* **49**, 31–42 (2016).
 - [14] David Awschalom, Karl K. Berggren, Hannes Bernien, Sunil Bhave, Lincoln D. Carr, Paul Davids, Sophia E. Economou, Dirk Englund, Andrei Faraon, Martin Fejer, Saikat Guha, Martin V. Gustafsson, Evelyn Hu, Liang Jiang, Jungsang Kim, Boris Korzh, Prem Kumar, Paul G. Kwiat, Marko Lončar, Mikhail D. Lukin, David A.B. Miller, Christopher Monroe, Sae Woo Nam, Prineha Narang, Jason S. Orcutt, Michael G. Raymer, Amir H. Safavi-Naeini, Maria Spiropulu, Kartik Srinivasan, Shuo Sun, Jelena Vučković, Edo Waks, Ronald Walsworth, Andrew M. Weiner, and Zheshe Zhang, “Development of quantum interconnects (quics) for next-generation information technologies,” *PRX Quantum* **2**, 017002 (2021).
 - [15] C. P. Sun, L. F. Wei, Yu-xi Liu, and Franco Nori, “Quantum transducers: Integrating transmission lines and nanomechanical resonators via charge qubits,” *Phys. Rev. A* **73**, 022318 (2006).
 - [16] Mohammad Mirhosseini, Alp Sipahigil, Mahmoud Kalae, and Oskar Painter, “Superconducting qubit to optical photon transduction,” *Nature* **588**, 599–603 (2020).
 - [17] Moritz Forsch, Robert Stockill, Andreas Wallucks, Igor Marinković, Claus Gärtner, Richard A. Norte, Frank van Otten, Andrea Fiore, Kartik Srinivasan, and Simon Gröblacher, “Microwave-to-optics conversion using a mechanical oscillator in its quantum ground state,” *Nature Physics* **16**, 69–74 (2020).
 - [18] K. G. Fedorov *et al.*, “Experimental quantum teleportation of propagating microwaves,” *Sci. Adv.* **7**, eabk0891 (2021).
 - [19] S. Pogorzalek *et al.*, “Secure quantum remote state preparation of squeezed microwave states,” *Nat. Commun.* **10**, 2604 (2019).
 - [20] P. Magnard, S. Storz, P. Kurpiers, J. Schär, F. Marxer, J. Lütolf, T. Walter, J.-C. Besse, M. Gabureac, K. Reuer, A. Akin, B. Royer, A. Blais, and A. Wallraff, “Microwave quantum link between superconducting circuits housed in spatially separated cryogenic systems,” *Phys. Rev. Lett.* **125**, 260502 (2020).
 - [21] Simon Storz, Josua Schär, Anatoly Kulikov, Paul Magnard, Philipp Kurpiers, Janis Lütolf, Theo Walter, Adrian Copetudo, Kevin Reuer, Abdulkadir Akin, Jean-Claude Besse, Mihai Gabureac, Graham J. Norris, Andrés Rosario, Ferran Martin, José Martinez, Waldimar Amaya, Morgan W. Mitchell, Carlos Abellan,

- Jean-Daniel Bancal, Nicolas Sangouard, Baptiste Royer, Alexandre Blais, and Andreas Wallraff, “Loophole-free bell inequality violation with superconducting circuits,” *Nature* **617**, 265–270 (2023).
- [22] Herbert B. Callen and Theodore A. Welton, “Irreversibility and generalized noise,” *Phys. Rev.* **83**, 34–40 (1951).
- [23] Ryogo Kubo, “Statistical-mechanical theory of irreversible processes. i. general theory and simple applications to magnetic and conduction problems,” *Journal of the Physical Society of Japan* **12**, 570–586 (1957), <https://doi.org/10.1143/JPSJ.12.570>.
- [24] A Marx, J Hoess, and K Uhlig, “Dry Dilution Refrigerator for Experiments on Quantum Effects in the Microwave Regime,” *ArXiv e-prints* (2014), 1412.3619.
- [25] The coaxial cables and related superconducting joints for connection have been developed and provided by **KEYCOM Corp.**
- [26] T. Poole, T. Foster, and A. J. Matthews, “Gas-gap heat switches with negative room temperature conductor separation and their application to ultra-low temperature platforms,” *Cryogenics* **130**, 103632 (2023).
- [27] G. Batey, M. Buehler, M. Cuthbert, T. Foster, A.J. Matthews, G. Teleberg, and A. Twin, “Integration of superconducting magnets with cryogen-free dilution refrigerator systems,” *Cryogenics* **49**, 727–734 (2009).
- [28] M. Wallquist, V. S. Shumeiko, and G. Wendin, “Selective coupling of superconducting charge qubits mediated by a tunable stripline cavity,” *Phys. Rev. B* **74**, 224506 (2006), [arXiv:0608209 \[cond-mat\]](https://arxiv.org/abs/0608209).
- [29] T. Yamamoto *et al.*, “Flux-driven josephson parametric amplifier,” *Appl. Phys. Lett.* **93**, 042510 (2008).
- [30] L Zhong, E P Menzel, R Di Candia, P Eder, M Ihmig, A Baust, M Haeberlein, E Hoffmann, K Inomata, T Yamamoto, Y Nakamura, E Solano, F Deppe, A Marx, and R Gross, “Squeezing with a flux-driven josephson parametric amplifier,” *New J. Phys.* **15**, 125013 (2013).
- [31] T Yamamoto, K Koshino, and Y Nakamura, “Parametric amplifier and oscillator based on josephson junction circuitry,” in *Principles and Methods of Quantum Information Technologies*, edited by Yoshihisa Yamamoto and Kouichi Semba (Springer Japan, Tokyo, 2016) pp. 495–513.
- [32] M. Mariantoni, E. P. Menzel, F. Deppe, M. Á. Araque Caballero, A. Baust, T. Niemczyk, E. Hoffmann, E. Solano, A. Marx, and R. Gross, “Planck spectroscopy and quantum noise of microwave beam splitters,” *Phys. Rev. Lett.* **105**, 133601 (2010).
- [33] Stefan Pogorzalek, Kirill G. Fedorov, Ling Zhong, Jan Goetz, Friedrich Wulschner, Michael Fischer, Peter Eder, Edwar Xie, Kunihiro Inomata, Tsuyoshi Yamamoto, Yasunobu Nakamura, Achim Marx, Frank Deppe, and Rudolf Gross, “Hysteretic flux response and nondegenerate gain of flux-driven josephson parametric amplifiers,” *Phys. Rev. Applied* **8**, 024012 (2017).
- [34] M. Renger, S. Pogorzalek, Q. Chen, Y. Nojiri, K. Inomata, Y. Nakamura, *et al.*, “Beyond the standard quantum limit for parametric amplification of broadband signals,” *Npj Quantum Inf.* **7**, 160 (2021).
- [35] M.R. Perelshtein, K.V. Petrovnin, V. Vesterinen, S. Hamedani Raja, I. Lilja, M. Will, A. Savin, S. Simbierowicz, R.N. Jabdaraghi, J.S. Lehtinen, L. Grönberg, J. Hassel, M.P. Prunnila, J. Govenius, G.S. Paraoanu, and P.J. Hakonen, “Broadband continuous-variable entanglement generation using a kerr-free josephson meta-material,” *Phys. Rev. Appl.* **18**, 024063 (2022).
- [36] E. P. Menzel, R. Di Candia, F. Deppe, P. Eder, L. Zhong, M. Ihmig, M. Haeberlein, A. Baust, E. Hoffmann, D. Ballester, K. Inomata, T. Yamamoto, Y. Nakamura, E. Solano, A. Marx, and R. Gross, “Path entanglement of continuous-variable quantum microwaves,” *Phys. Rev. Lett.* **109**, 250502 (2012).
- [37] S. L. Braunstein and P. van Loock, “Quantum information with continuous variables,” *Rev. Mod. Phys.* **77**, 513–577 (2005).
- [38] K. G. Fedorov, S. Pogorzalek, U. Las Heras, M. Sanz, P. Yard, P. Eder, M. Fischer, J. Goetz, E. Xie, K. Inomata, Y. Nakamura, R. Di Candia, E. Solano, A. Marx, F. Deppe, and R. Gross, “Finite-time quantum entanglement in propagating squeezed microwaves,” *Scientific Reports* **8**, 6416 (2018).
- [39] Asher Peres, “Separability criterion for density matrices,” *Phys. Rev. Lett.* **77**, 1413–1415 (1996).
- [40] T. Yu and J. H. Eberly, “Sudden death of entanglement,” *Science* **323**, 598–601 (2009).
- [41] M. Renger, S. Pogorzalek, F. Fesquet, K. Honasoge, F. Kronowetter, Q. Chen, Y. Nojiri, K. Inomata, Y. Nakamura, A. Marx, F. Deppe, R. Gross, and K. G. Fedorov, “Flow of quantum correlations in noisy two-mode squeezed microwave states,” *Phys. Rev. A* **106**, 052415 (2022).
- [42] J. P. Turneaure and Ira Weissman, “Microwave surface resistance of superconducting niobium,” *Journal of Applied Physics* **39**, 4417–4427 (1968), <https://doi.org/10.1063/1.1656986>.
- [43] J. Bardeen, L. N. Cooper, and J. R. Schrieffer, “Theory of superconductivity,” *Phys. Rev.* **108**, 1175–1204 (1957).
- [44] J. Agustí, Y. Minoguchi, J. M. Fink, and P. Rabl, “Long-distance distribution of qubit-qubit entanglement using gaussian-correlated photonic beams,” *Phys. Rev. A* **105**, 062454 (2022).
- [45] Nicolas Didier, Jérémie Guillaud, Shyam Shankar, and Mazhar Mirrahimi, “Remote entanglement stabilization and concentration by quantum reservoir engineering,” *Phys. Rev. A* **98**, 012329 (2018).
- [46] Ulrik L. Andersen, Jonas S. Neergaard-Nielsen, Peter van Loock, and Akira Furusawa, “Hybrid discrete - and continuous-variable quantum information,” *Nature Physics* **11**, 713–719 (2015).
- [47] Shuntaro Takeda, Takahiro Mizuta, Maria Fuwa, Peter van Loock, and Akira Furusawa, “Deterministic quantum teleportation of photonic quantum bits by a hybrid technique,” *Nature* **500**, 315–318 (2013).
- [48] Robert Lasenby, “Microwave cavity searches for low-frequency axion dark matter,” *Phys. Rev. D* **102**, 015008 (2020).
- [49] T. Braine *et al.* (ADMX Collaboration), “Extended search for the invisible axion with the axion dark matter experiment,” *Phys. Rev. Lett.* **124**, 101303 (2020).
- [50] KEYCOM Corp. 3-40-2 Minamitsuka, Toshima-ku Tokyo 170-0005 Japan.
- [51] F. Pobell, *Matter and Methods at Low Temperatures* (Springer Berlin Heidelberg, 2007).
- [52] E. D. Marquardt, J. P. Le, and R. Radebaugh, “Cryogenic material properties database,” *Presented at the 11th International Cryocooler Conference June 20-22, 2000 Keystone, Co* (2000).
- [53] N. Simon, Elizabeth Drexler, and R. Reed, “Properties of copper and copper alloys at cryogenic temperatures,”

- NIST Monograph **177** (1992).
- [54] Rudolf Gross and Achim Marx, *Festkörperphysik* (Oldenbourg Verlag, München, 2012).
 - [55] Y.S. Touloukian, *Thermal Expansion: Metallic Elements and Alloys*, TPRC data series (Springer US, 1975).
 - [56] G.B. Arfken, H.J. Weber, and F.E. Harris, *Mathematical Methods for Physicists: A Comprehensive Guide* (Elsevier Science, 2012).
 - [57] E. Gottardi, G. Bianchini, I. Peroni, A. Peruzzi, and G. Ventura, “Thermal conductivity of polyetheretherketone at low,” in *Proc. 8th Int. Symp. on Temperature and Thermal Measurements in Industry and Science (Berlin)* (2001) p. 1151.
 - [58] Andrey V. Timofeev, Meri Helle, Matthias Meschke, Mikko Möttönen, and Jukka P. Pekola, “Electronic refrigeration at the quantum limit,” *Phys. Rev. Lett.* **102**, 200801 (2009).
 - [59] Dietrich Einzel, “Spin-independent transport parameters for superfluid $^3\text{He-B}$,” *Journal of Low Temperature Physics* **54**, 427–474 (1984).
 - [60] D. Einzel, “Interpolation of bcs response functions,” *Journal of Low Temperature Physics* **130**, 493–508 (2003).
 - [61] Dietrich Einzel, “Universal parameters in the response of unconventional superconductors,” *Journal of Low Temperature Physics* **126**, 867–879 (2002).
 - [62] Bernhard Mühlshlegel, “Die thermodynamischen funktionen des supraleiters,” *Zeitschrift für Physik* **155**, 313–327 (1959).
 - [63] G Krainz and Dietrich Hagedorn, “Quench protection and powering in a string of superconducting magnets for the large hadron collider,” (1997).
 - [64] A. Kushino, S. Kasai, S. Kohjiro, S. Shiki, and M. Ohkubo, “Development of superconducting coaxial cables for cryogenic detectors,” *Journal of Low Temperature Physics* **151**, 650–654 (2008).
 - [65] Philipp Kurpiers, Theodore Walter, Paul Magnard, Yves Salathe, and Andreas Wallraff, “Characterizing the attenuation of coaxial and rectangular microwave-frequency waveguides at cryogenic temperatures,” *EPJ Quantum Technol.* **4**, 8 (2017).
 - [66] M. Göppl, A. Fragner, M. Baur, R. Bianchetti, S. Filipp, J. M. Fink, P. J. Leek, G. Puebla, L. Steffen, and A. Wallraff, “Coplanar waveguide resonators for circuit quantum electrodynamics,” *J. Appl. Phys.* **104**, 113904 (2008).
 - [67] D.M. Pozar, *Microwave Engineering*, 4th ed. (John Wiley & Sons, Hoboken, 2011).
 - [68] Qi-Ming Chen, Meike Pfeiffer, Matti Partanen, Florian Fesquet, Kedar E. Honasoge, Fabian Kronowetter, Yuki Nojiri, Michael Renger, Kirill G. Fedorov, Achim Marx, Frank Deppe, and Rudolf Gross, “Scattering coefficients of superconducting microwave resonators. i. transfer matrix approach,” *Phys. Rev. B* **106**, 214505 (2022).
 - [69] Valerio Scarani, Helle Bechmann-Pasquinucci, Nicolas J. Cerf, Miloslav Dušek, Norbert Lütkenhaus, and Momtchil Peev, “The security of practical quantum key distribution,” *Rev. Mod. Phys.* **81**, 1301–1350 (2009).
 - [70] C. Enss and S. Hunklinger, *Low-Temperature Physics*, SpringerLink: Springer e-Books (Springer Berlin Heidelberg, 2005).
 - [71] T.O. Klaassen, J.H. Blok, J.N. Hovenier, G. Jakob, D. Rosenthal, and K.J. Wildeman, “Absorbing coatings and diffuse reflectors for the herschel platform submillimeter spectrometers hifi and pacs,” in *Proceedings, IEEE Tenth International Conference on Terahertz Electronics* (2002) pp. 32–35.
 - [72] Y.A. Çengel and A.J. Ghajar, *Heat and Mass Transfer: Fundamentals & Applications*, Asia Higher Education Engineering/Computer Science Mechanica (McGraw Hill Education, 2015).
 - [73] J.G.M. Kuerten, C.A.M. Castelijns, A.T.A.M. de Waele, and H.M. Gijsman, “Thermodynamic properties of liquid ^3He - ^4He mixtures at zero pressure for temperatures below 250 mk and ^3He concentrations below 8%,” *Cryogenics* **25**, 419–443 (1985).
 - [74] Gunaranjan Chaudhry and J. G. Brisson, “Thermodynamic properties of liquid ^3He - ^4He mixtures between 0.15k and 1.8k,” *Journal of Low Temperature Physics* **155**, 235–289 (2009).
 - [75] J.V. Beck, K.D. Cole, A. Haji-Sheikh, and B. Litkouhl, *Heat Conduction Using Green's Function*, Series in Computational Methods and Physical Processes in Mechanics and Thermal Sciences (Taylor & Francis, 1992).
 - [76] R. G. Ross, “Cryocooler load increase due to external contamination of low- ϵ cryogenic surfaces,” in *Cryocoolers 12*, edited by Ronald G. Ross (Springer US, Boston, MA, 2003) pp. 727–736.
 - [77] M.Q. Brewster, *Thermal Radiative Transfer and Properties*, A Wiley-Interscience publication (Wiley, 1992).
 - [78] O. A. Alduchov and R. E. Eskridge, *Improved Magnus’ form approximation of saturation vapor pressure*, Tech. Rep. (United States, 1997) research Org.: Department of Commerce, Asheville, NC (United States).
 - [79] “Average humidity in Munich (Bavaria)”, <https://weather-and-climate.com/average-monthly-Humidity-perc,munich,Germany>, Accessed: 2022-12-15.
 - [80] P. Sturm, M. Leuenberger, C. Sirignano, R. E. M. Neubert, H. A. J. Meijer, R. Langenfelds, W. A. Brand, and Y. Tohjima, “Permeation of atmospheric gases through polymer o-rings used in flasks for air sampling,” *Journal of Geophysical Research: Atmospheres* **109** (2004), <https://doi.org/10.1029/2003JD004073>.
 - [81] Simon C J Kingsley, H Jones, A Twin, H Agrawal, A Matthews, G J Batey, and M Cuthbert, “Review of recently supplied oxford instruments uhv/ult cryostats,” *Journal of Physics: Conference Series* **400**, 052012 (2012).
 - [82] K. G. Fedorov *et al.*, “Displacement of propagating squeezed microwave states,” *Phys. Rev. Lett.* **117**, 020502 (2016).